

Title	Large-area growth of MoS ₂ at temperatures compatible with integrating back-end-of-line functionality
Authors	Lin, Jun;Monaghan, Scott;Sakhuja, Neha;Gity, Farzan;Kumar Jha, Ravindra;Coleman, Emma M.;Connolly, James;Cullen, Conor P.;Walsh, Lee A.;Mannarino, Teresa;Schmidt, Michael;Sheehan, Brendan;Duesberg, Georg S.;McEvoy, Niall;Bhat, Navakanta;Hurley, Paul K.;Povey, Ian M.;Bhattacharjee, Shubhadeep
Publication date	2020-12-24
Original Citation	Lin, J., Monaghan, S., Sakhuja, N., Gity, F., Kumar Jha, R., Coleman, E. M., Connolly, J., Cullen, C. P., Walsh, L. A., Mannarino, T., Schmidt, M., Sheehan, B., Duesberg, G. S., McEvoy, N., Bhat, N., Hurley, P. K., Povey, I. M. and Bhattacharjee, S. (2021) 'Large-area growth of MoS ₂ at temperatures compatible with integrating back-end-of-line functionality', 2D Materials, 8(2), 025008 (20pp). doi: 10.1088/2053-1583/abc460
Type of publication	Article (peer-reviewed)
Link to publisher's version	10.1088/2053-1583/abc460
Rights	© 2020, IOP Publishing Ltd. This is an author-created, un-copyedited version of an article accepted for publication in 2D Materials. The publisher is not responsible for any errors or omissions in this version of the manuscript or any version derived from it. The Version of Record is available online at: https://iopscience.iop.org/article/10.1088/2053-1583/abc460 - https://creativecommons.org/licenses/by-nc-nd/4.0/
Download date	2025-05-08 18:43:02
Item downloaded from	https://hdl.handle.net/10468/12348



University College Cork, Ireland
Coláiste na hOllscoile Corcaigh

ACCEPTED MANUSCRIPT

Large-Area Growth of MoS₂ at Temperatures Compatible with Integrating Back-End-of-Line Functionality

To cite this article before publication: Jun Lin *et al* 2020 *2D Mater.* in press <https://doi.org/10.1088/2053-1583/abc460>

Manuscript version: Accepted Manuscript

Accepted Manuscript is “the version of the article accepted for publication including all changes made as a result of the peer review process, and which may also include the addition to the article by IOP Publishing of a header, an article ID, a cover sheet and/or an ‘Accepted Manuscript’ watermark, but excluding any other editing, typesetting or other changes made by IOP Publishing and/or its licensors”

This Accepted Manuscript is © 2020 IOP Publishing Ltd.

During the embargo period (the 12 month period from the publication of the Version of Record of this article), the Accepted Manuscript is fully protected by copyright and cannot be reused or reposted elsewhere.

As the Version of Record of this article is going to be / has been published on a subscription basis, this Accepted Manuscript is available for reuse under a CC BY-NC-ND 3.0 licence after the 12 month embargo period.

After the embargo period, everyone is permitted to use copy and redistribute this article for non-commercial purposes only, provided that they adhere to all the terms of the licence <https://creativecommons.org/licenses/by-nc-nd/3.0>

Although reasonable endeavours have been taken to obtain all necessary permissions from third parties to include their copyrighted content within this article, their full citation and copyright line may not be present in this Accepted Manuscript version. Before using any content from this article, please refer to the Version of Record on IOPscience once published for full citation and copyright details, as permissions will likely be required. All third party content is fully copyright protected, unless specifically stated otherwise in the figure caption in the Version of Record.

View the [article online](#) for updates and enhancements.

Large-Area Growth of MoS₂ at Temperatures Compatible with Integrating Back-End-of-Line Functionality

Jun Lin¹, Scott Monaghan¹, Neha Sakhuja², Farzan Gity¹, Ravindra Kumar Jha³, Emma M. Coleman¹, James Connolly¹, Conor P. Cullen⁴, Lee A. Walsh¹, Teresa Mannarino¹, Michael Schmidt¹, Brendan Sheehan¹, Georg S. Duesberg^{4,5}, Niall McEvoy⁴, Navakanta Bhat², Paul K. Hurley^{1,6}, Ian M. Povey¹ and Shubhadeep Bhattacharjee¹

¹ Tyndall National Institute, University College Cork, Lee Maltings Complex, Cork, T12R5CP, Ireland

² Centre for Nanoscience and Engineering, Indian Institute of Science, Bangalore, India

³ Nano Bio Sensors Group, CSIR-Central Electronics Engineering Research Institute (CEERI), Pilani, Rajasthan, India

⁴ CRANN and AMBER Research Centres and School of Chemistry, Trinity College Dublin, D02PN40, Ireland

⁵ Institute of Physics, EIT 2, Faculty of Electrical Engineering and Information Technology, Universität der Bundeswehr München, Werner Heisenberg Weg 39, 85577 Neubiberg, Germany

⁶ School of Chemistry, University College Cork, Cork, Ireland

E-mail: jun.lin@tyndall.ie

Abstract

Direct growth of transition metal dichalcogenides over large areas within the back-end-of-line (BEOL) thermal budget limit of silicon integrated circuits is a significant challenge for 3D heterogeneous integration. In this work, we report on the growth of MoS₂ films (~1–10 nm) on SiO₂, amorphous-Al₂O₃, c-plane sapphire, and glass substrates achieved at low temperatures (350–550 °C) by chemical vapor deposition in a manufacturing-compatible 300 mm atomic layer deposition reactor. We investigate the MoS₂ films as a potential material solution for BEOL logic, memory and sensing applications. Hall-effect/4-point measurements indicate that the ~10 nm MoS₂ films exhibit very low carrier concentrations (10¹⁴–10¹⁵ cm⁻³), high resistivity, and Hall mobility values of ~0.5–17 cm² V⁻¹ s⁻¹, confirmed by transistor and resistor test device results. MoS₂ grain boundaries and stoichiometric defects resulting from the low thermal budget growth, while detrimental to lateral transport, can be leveraged for the integration of memory and sensing functions. Vertical transport memristor structures (Au/MoS₂/Au) incorporating ~3 nm thick MoS₂ films grown at 550 °C (~0.75 hours) show memristive switching and a stable memory window of 10⁵ with a retention time > 10⁴ seconds, between the high-low resistive states. The switching set and reset voltages in these memristors demonstrate a significant reduction compared to memristors fabricated from pristine, single-crystalline MoS₂ at higher temperatures, thereby reducing the energy needed for operation. Furthermore, interdigitated electrode-based gas sensors fabricated on ~5 nm thick 550 °C-grown (~1.25 hours) MoS₂ films show excellent selectivity and sub-ppm sensitivity to NO₂ gas, with a notable self-recovery at room temperature. The demonstration of large-area MoS₂ direct growth at and below the BEOL thermal budget limit, alongside memristive and gas sensing functionality, advances a key enabling technology objective in emerging materials and devices for 3D heterogeneous integration.

Keywords: MoS₂, 300 mm CVD, BEOL thermal budget, 3D heterogeneous integration, Hall-effect, memristors, gas sensors

1. Introduction

Graphene is a pioneer in two-dimensional (2D) materials. In addition to its applications in flexible electronics where large scale synthesis has been reported, i.e. in a roll-to-roll production [1], graphene can provide potential applications at the back-end-of-line (BEOL) of conventional integrated circuits [2, 3]. Recently, transition metal dichalcogenides (TMDs) have emerged from the graphene initiatives due to the diverse functionality offered by the incorporation of this class of 2D layered material. More specifically, TMDs can be engineered to provide bandgap tunability and therefore exhibit electronic properties from semimetals to wide bandgap semiconductors, thus opening up new opportunities in applications from optical and electronic devices (e.g. memory and logic), to sensors and medical electronics [4-12].

While initial studies of TMDs were performed on exfoliated flakes, obtained from natural and synthetic crystals, in recent years the focus has extended to studies of large-area growth methods to assess practical manufacturability of materials and devices. Of particular interest for 3D heterogeneous integration is the rapid growth of TMD materials at $\leq \sim 550$ °C, as this opens up the possibility of integrating TMD-based devices at the BEOL [13-16], with the potential to provide a low-temperature growth semiconductor for logic, memory or sensing functionality above the temperature-sensitive complementary metal-oxide-semiconductor (CMOS) circuitry. More-than-Moore heterogeneous integration with BEOL compatibility is a key enabling technology that opens up avenues for supplementing ‘dimensional scaling’ with ‘functional scaling’. Given the constraints of a low thermal budget, the requirement of wide functional diversity supersedes the need for high performance [17-20]. It is noted that low-temperature growth of semiconducting materials is also of relevance to other applications with temperature-sensitive substrates, such as flexible electronics and displays.

Among the TMD options, MoS₂ has drawn much attention due to its thickness-dependent bandgap [5]. Moreover, field-effect transistors (FETs) based on exfoliated MoS₂ have demonstrated excellent field modulation with high On/Off current ratio ($> 10^5$ [21], 10^6 [7], 10^8 [22] and up to $\sim 10^9$ [23]), small subthreshold swing (74 mV dec⁻¹ [22], 70 mV dec⁻¹ [24] and 65 mV dec⁻¹ [7]), and high mobility values (> 100 cm² V⁻¹ s⁻¹ [24] and ~ 200 cm² V⁻¹ s⁻¹ [22]). Chemical vapor deposition (CVD) [25-42] and atomic layer deposition (ALD) [43-51] are leading candidates for controlled wafer-level growth of MoS₂,

although limited grain size can inhibit lateral transport properties compared to flakes exfoliated from crystals. While one monolayer MoS₂ may theoretically provide the highest performance, production capability for high quality, single crystal MoS₂ is at its infancy, and present methods rarely produce high performance device grade material, despite the high process temperatures, which are non-compatible with the BEOL thermal budget limit. Recent work has demonstrated high temperature ($>$ BEOL thermal budget) CVD-growth of MoS₂ on sacrificial 300 mm wafers with subsequent film transfer for device fabrication [25]. Moreover, it should be noted that caveats abound in the interpretation of TMD properties, and achieving reliable electronics-grade devices for logic applications is extremely challenging [52].

In addition to in-plane switching characteristics for logic applications, 2D semiconductors such as MoS₂ offer unique advantages for expanding device functionalities to resistive switching (memristive action) and gas-sensing applications. The use of 2D materials as an active layer for resistive switching presents two key merits over conventional oxides. The thickness non-uniformity associated with the scaling of the active material can be completely eliminated even for sub-nm lengths by using a monolayer of TMD. Subsequently, this could result in drastic improvements in the density of integration, reliability and power dissipation. In this regard, memristors fabricated using CVD-grown MoS₂ and other materials have been reported in lateral [53, 54] and vertical [55-59] structures. Furthermore, MoS₂ has been extensively studied for gas sensing applications [60-73]. In recent years, several groups have demonstrated MoS₂-based NO₂ sensors for detection at ppm levels [64, 74]. Zhao *et al.* prepared 2D MoS₂ using a low temperature CVD process, which exhibited a 97% response towards 25 ppm NO₂ at room temperature (RT) [64]. Recently, a NO₂ gas sensor based on a CVD-grown MoS₂ FET displayed significant performance at sub-ppm (20 ppb) levels [75]. However, these sensors suffer from a drawback of sluggish recovery at RT. Subsequent research has been directed towards improving the recovery of the sensor by employing external sources such as thermal annealing in the range of 100 °C to 200 °C [60, 76, 77]. UV and red-light illumination of MoS₂ channels have also emerged as alternative strategies to improve the recovery rate of the sensors at ppm levels. Herein, UV light releases adsorbed oxygen ions from the surface of MoS₂. This in turn allows NO₂ molecules to interact with conducting electrons in the MoS₂ channel and accelerates the desorption rate of adsorbed NO₂ molecules [67].

For 3D heterogeneous integration, it is necessary to restrict the thermal budget associated with the growth process, including pre-deposition substrate annealing, and any subsequent post-deposition annealing, to be below the BEOL thermal budget limit, as otherwise, measureable degradation is observed in the underlying transistors in the CMOS circuitry [15]. However, in order to achieve high-quality MoS₂, a high-temperature deposition, or a high-temperature annealing either pre- or post-deposition, is usually needed [29-41, 47-51]; and many reports are at high temperatures ≥ 1000 °C for several hours [39-41, 51]. This is a common approach widely used to realise logic functionality. There is a limited number of reports on CVD and ALD of MoS₂ processed at temperatures ≤ 550 °C in the literature [26-28, 43-46], and we will explore each of these in the context of our work.

As described, significant progress has been made to date in the development of large-area growth processes for MoS₂. However, reports of CVD MoS₂ growth at low temperature, combined with associated device performance are limited to date [78]. This forms the motivation for our study which explores the growth of MoS₂ in the temperature range of 350 °C to 550 °C along with memory and sensor devices formed using the MoS₂ films, with no high-temperature annealing prior to or after the growth process. Considering the upper limit for the MoS₂ growth temperature and time in this study, a guideline is provided based on a detailed study exploring the impact of the annealing thermal budget on fully depleted silicon-on-insulator devices, which indicates negligible degradation of *n* and *p* channel metal-oxide-semiconductor FET (MOSFET) performance for anneals up to two thermal budget regimes: (1) 550 °C/2 hours; and (2) 500 °C/5 hours [15]. The present definition of the BEOL thermal budget limit for monolithic heterogeneous 3D integration, in terms of the different process temperatures and the different process times that have been experimentally verified to be close to, but within, the BEOL thermal budget limit, makes it difficult to compare against when, for example, other works have used different process temperatures and different process times. There is an uncertainty therefore on thermal budget compatibility if a different thermal budget temperature and time set are employed that does not match those already experimentally verified. This vagueness could be removed if a single caloric value in terms of a heat transfer energy equation, and as a function of the process temperature and process time, could fully describe the BEOL thermal budget regime. While deriving such a description would likely require a dedicated study, and is outside the scope of this work, we discuss the topic further in the Supporting Information in the context of figure S1. In relation to the upper limit of the thermal budget, and considering the very significant gains that can be achieved in terms of energy consumption and latency through 3D integration, it is worth noting that the underlying silicon circuitry could also be engineered to sustain a higher

thermal budget during the processing of subsequent logic, memory or sensing layers [79].

In this work, the growth of different MoS₂ thicknesses is initially performed at 550 °C for 0.3–2.5 hours, which is approximately at and below the maximum BEOL thermal budget limit. Furthermore, MoS₂ is achieved at 450 °C (2.5 or 6 hours) and 350 °C (2.5 hours), which are also approximately at and below the thermal budget limit for the BEOL. The structural, chemical and electronic properties are reported, including results of Hall-effect analysis of MoS₂ grown at 350–550 °C which has rarely been reported in the literature. Following analysis of the film properties, the behaviour of the low-temperature grown MoS₂ films in vertical memristive devices and gas sensors is reported.

2. Experimental Details

2.1 CVD of MoS₂

CVD of MoS₂ was performed in a commercial 300 mm ALD reactor, fitted with a showerhead, employing Mo(CO)₆ (99.99%, Versum Materials) and 1% H₂S (99.999%) in Ar (Air Products) as the precursors. The reactor temperature was varied between 350 °C and 550 °C and the chamber pressure maintained at ~ 2.2 Torr by an N₂ carrier flow of 150 standard cubic centimeters per minute (sccm). Precursor flux of the Mo source was determined by the source temperature (28–50 °C) and the H₂S flow was set at 10 or 20 sccm of the 1% gas mix. Growth was achieved on a selection of substrates including: SiO₂ (85 nm) on Si (p++), c-plane sapphire, glass, and amorphous alumina (a-Al₂O₃, ~ 30 nm grown by ALD) on c-plane sapphire and on glass. At the reduced growth temperatures of 450 °C and 350 °C, a variation of precursor flow was investigated by doubling H₂S flow or reducing the Mo(CO)₆ flux by lowering the Mo(CO)₆ ampule temperature. The primary aim of these variations was to increase the sulfur/molybdenum ratio in order to minimise sulfur deficiencies in lower temperature grown films. The growth time was ~ 2.5 hours for all nominally 10 nm MoS₂ thicknesses, except for the reduced Mo(CO)₆ flow condition (~ 6 hours).

2.2 Structural and Chemical Analysis Setup

The cross-sectional transmission electron microscopy (XTEM) samples were prepared using a Dual Beam Focused Ion Beam (FIB) FEI Helios NanoLab 600i. A 50 nm carbon layer and a 300 nm platinum layer were deposited by e-beam evaporation followed by a 2 μ m thick carbon layer by ion-beam for protection before the milling process. The lamella was thinned down to less than 200 nm thickness followed by polishing (final thinning at 93 pA 30 kV, final polish 2 kV 28 pA). For the plan-view of the MoS₂, the film was transferred from a SiO₂(85 nm)/Si substrate onto a TEM grid using 2M sodium hydroxide solution. Following MoS₂ film

release from the grown substrate, the floating film was 'fished' out onto a TEM grid. TEM analysis was performed using a JEOL JEM-2100 at 200 kV in bright field mode. Raman spectra were acquired using a WITec Alpha 300R with a 532 nm excitation laser to investigate the MoS₂ formed on different substrates. A Renishaw RAMAN inVia (laser 514 nm) was also used for Raman spatial mapping measurements on different thicknesses of MoS₂ on various substrates. X-ray photoelectron spectroscopy (XPS) spectra were generally recorded under ultra-high vacuum conditions ($< 10^{-8}$ mbar) using a VG Scientific ESCA-lab MkII system using Al K α x-rays and an analyser pass energy of 20 eV. Core-level spectra were fitted with CasaXPS software using Gaussian-Lorentzian line shapes, after subtraction of a Shirley background and charge correction to the C 1s at 284.8 eV. Confirmatory spectra were gathered using monochromated Al K α x-rays from an Omicron XM1000 MkII x-ray source and an Omicron EA125 energy analyser. An Omicron CN10 electron flood gun was used for charge compensation. A Philips X'Pert X-ray Diffractometer was used for the routine x-ray diffraction (XRD) measurements with a scan step size of 0.01° and 0.5 seconds per step comparing the MoS₂ growth on different substrates. Atomic force microscopy (AFM) measurements were performed using a Bruker Dimension Icon with SCANASYST-AIR AFM probes with a nominal tip radius of 2 nm. AFM scanning employed Bruker's PeakForce Tapping. Scanned sites measured 2 $\mu\text{m} \times 2 \mu\text{m}$ with 1024 samples per line with different sites tested per sample. Values of roughness (R_q) over the full scan area was compared to selected regions within the scan area to assess whether the reported R_q values were consistent across different sites.

2.3 Device Fabrication

1 mm \times 1 mm square Van der Pauw (VdP) Hall structures were patterned using SF₆-based inductively coupled plasma (ICP) etch and metallised with Ni/Au tracks/pads. Back-gated FETs were fabricated by patterning source and drain Ni/Au metal contacts followed by the same ICP etch process to form the channel. All metal contacts in the circular transmission line method (c-TLM), patterned Hall and the back-gated transistor devices were formed using standard photolithography followed by e-beam evaporation of Ni (20 nm) / Au (200 nm) and a lift-off process. For the memristors, the bottom electrodes were patterned on an 85 nm SiO₂/Si substrate using optical lithography followed by 30 nm Au deposition and lift-off. Next, the MoS₂ grown (550 °C, 10 sccm 1% H₂S, 0.75 hours, ~ 3 nm) on the sapphire substrate was transferred onto the patterned SiO₂ sample using standard polymer-based transfer techniques using polymethyl methacrylate (PMMA). This was followed by patterning the MoS₂ into well-defined squares by SF₆ etch chemistry and lithography definition and deposition of 30 nm thick Au top electrodes. For gas sensing, each sensor device has 50 standard interdigitated electrodes

(IDEs) that are 5 μm wide and have a 5 μm gap between each, and were defined on ~ 5 nm MoS₂ films (grown at 550 °C, 10 sccm 1% H₂S, for 1.25 hours on sapphire) using optical lithography. This was followed by deposition of Ti/Au (10 nm / 100 nm) using e-beam evaporation. Subsequently, the MoS₂ was patterned through SF₆ etch chemistry such that the film is only present in the areas covered by IDEs and not at the probing pads.

2.4 Hall-effect and 4P Resistivity Methods

The Hall-effect, 4-point and 2-point resistance (Hall/4P/2P) measurements were performed in a LakeShore Model 8404 DC/AC Hall-Effect Measurement System fitted with a high resistance unit (up to 200 G Ω in DC mode). System calibration on the two-geometry setups was verified prior to all measurements. The samples were either VdP 1 cm \times 1 cm, or patterned 1 mm \times 1 mm, MoS₂ structures. Sheet resistivity values were measured from the 4P resistivity measurements, during which current reversal was performed to remove the thermal-electric voltage. The electromagnet can provide DC (up to ± 1.7 T) or AC (~ 1.28 T RMS at a frequency of 50 mHz and ~ 1.24 T RMS at 100 mHz) magnetic fields. The carrier type and sheet carrier concentration reported in this work were all obtained from RT DC magnetic field (at the maximum of ± 1.7 T) Hall-effect measurements, during which current reversal and field reversal were applied to remove the thermal-electric voltage and the misalignment voltage, respectively. For both the 2P and 4P resistances, and the DC Hall-effect measurements, indium foil was placed between the gold probes and MoS₂ film to reduce the contact resistance. The 2P results still include the high contact resistance, whereas the 4P results successfully remove the high contact resistance.

2.5 Setup for Transistors, c-TLMs and Memristors

The electrical measurements on back-gated transistors, c-TLMs and memristors were performed using either an Agilent 4156A or an Agilent B1500A semiconductor device analyser with a Cascade Microtech probe station (model Submit 12971B), in a dry air Faraday cage low noise environment.

2.6 Gas Sensing Setup

The gas sensing experiments were carried out in an in-house constructed setup which is also discussed in the previous work [80]. In brief, the setup constitutes a volumetric chamber connected to mass flow controllers, a thermocouple-based temperature controller and a Data Acquisition system (Keithley 2450). The IDE devices were probed inside the volumetric chamber and a DC bias of 5 V was provided during measurements. Standard commercial gas cylinders of highest purity were used during the measurements. Standard synthetic air was used to dilute these gases to achieve the desired

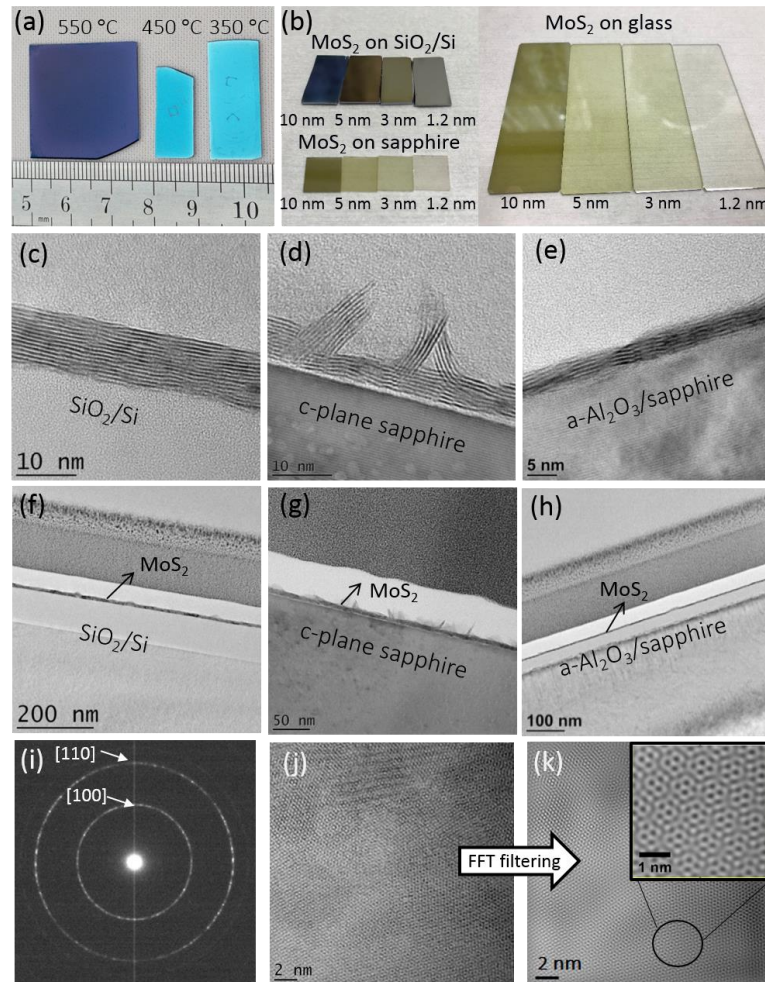


Figure 1. (a) 550/450/350 °C CVD-grown MoS₂ on SiO₂/Si substrates. Such coupons are placed throughout the chamber demonstrating that uniform and continuous film deposition is achievable across a 300 mm diameter. (b) Different MoS₂ thicknesses grown on SiO₂/Si (~2 cm × 1 cm), c-plane sapphire (~1 cm × 1 cm), and glass (7.5 cm × 2.5 cm) substrates. The thicknesses shown are nominal values assuming a linear growth rate. (c-e) HR-XTEM micrographs show polycrystalline and layered MoS₂ (550 °C, 10 sccm 1% H₂S, 2.5 hours) on SiO₂/Si, sapphire and a-Al₂O₃ (~30 nm)/sapphire. (f-h) Zoomed-out HR-XTEM micrographs of the MoS₂ on SiO₂/Si, sapphire and a-Al₂O₃ (~30 nm)/sapphire. (i) Electron diffraction pattern confirms the formation of polycrystalline MoS₂, where [100] and [110] are dominant orientations. (j) Plan-view HR-TEM of MoS₂ initially grown on SiO₂/Si substrate and transferred onto a TEM grid, showing the hexagonal structures of CVD-grown MoS₂. (k) FFT filtering produces a clear image of the hexagonal crystal structure.

concentrations. The standard synthetic air was also used to achieve the baseline resistance of the device.

3. Results and Discussion

3.1 Structural and Chemical Analysis

Figure 1(a) shows the ~10 nm MoS₂ grown at 350–550 °C on SiO₂/Si substrates, showing a lighter blue colour at decreased temperatures, likely due to increasing disorder and oxygen incorporation. Repeatability of the CVD process is found to be excellent. Such coupons are placed over the area of the 300 mm chamber and a uniform thickness is obtained

indicating that continuous MoS₂ films are achievable over a 300 mm diameter chamber with uniform thickness growth. By varying the growth time (550 °C, 10 sccm 1% H₂S), different thicknesses of MoS₂ are achieved (2.5 hours / 10 nm, 1.25 hours / 5 nm, 0.75 hours / 3 nm, 0.3 hours / 1.2 nm), as shown in figure 1(b) on SiO₂/Si, sapphire, and glass substrates, where colours go from almost transparent to increasingly opaque with increasing thickness. The nominal thicknesses are based on the 10 nm MoS₂ formed in 2.5 hours on SiO₂/Si, confirmed in figure 1(c) with high-resolution XTEM (HR-XTEM), with the assumption of a linear growth rate.

HR-XTEM micrographs of the MoS₂ grown at 550 °C on SiO₂/Si, sapphire and a-Al₂O₃/sapphire are shown in figure 1(c-e), and zoomed-out micrographs are shown in figure 1(f-h), confirming that polycrystalline and layered MoS₂ is formed continuously and uniformly on the substrates. The growth achieved on amorphous surfaces (SiO₂ and a-Al₂O₃) is similar, except for a reduced thickness of ~4–5 nm (i.e. ~3 monolayers/hour) on a-Al₂O₃/sapphire compared to ~9–10 nm (i.e. ~6 monolayers/hour) MoS₂ deposited on SiO₂/Si substrate. The growth of MoS₂ on c-plane sapphire also gives a reduced thickness of 5–6 nm (i.e. ~3–4 monolayers/hour), and presents more “out-of-plane” vertical growth features (which are excluded in the thickness estimation), compared to the growth on the amorphous surfaces of SiO₂ and a-Al₂O₃. This could be due to different nucleation and growth mechanisms, such as one via MoO_x [81]. To investigate further, MoS₂ grown on a SiO₂/Si substrate is transferred onto a TEM grid for plan-view HR-TEM analysis. The electron diffraction pattern shown in figure 1(i) confirms the formation of polycrystalline MoS₂, where [100] and [110] are the dominant orientations. Figure 1(j), which is a high resolution plan-view micrograph of MoS₂ on the TEM grid, shows the hexagonal structures of MoS₂ and the polycrystalline nature of the CVD-grown MoS₂. The HR-XTEM and plan-view HR-TEM micrographs indicate a small grain size of up to ~20 nm on the SiO₂/Si and a-Al₂O₃/sapphire substrates, and up to ~5 nm on c-plane sapphire, where the grain sizes are estimated based on the occurrence of out-of-plane features. Performing Fast Fourier Transform (FFT) filtering to the plan-view HR-TEM micrographs gives a clearer image of the hexagonal structures distributed into the film thickness, as illustrated in figure 1(k). It is notable that the MoS₂ growth in this work is very fast compared to a previous metal organic CVD (MOCVD) of MoS₂ of μm-scale grain size using Mo(CO)₆ and (C₂H₅)₂S at 550 °C reported by Kang *et al.*, in which 26 hours was needed for a complete one monolayer formation [28]. A rapid growth time is important in terms of reducing the thermal budget, but this comes at a cost of smaller grain sizes. In this work, although the growth at 550 °C is at the limit of the maximum temperature of the BEOL thermal budget limit [15], the rapid growth rate provides a significant trade-off.

Raman analysis on the MoS₂ deposited at 550 °C on all substrates in figure 2(a) shows a characteristic 2H-MoS₂ signal with well-defined E_{2g}¹ and A_{1g} peaks. There are some peaks in the range 150–250 cm⁻¹ which are likely to be related to oxygen incorporation, defects and grain boundary disorder [82, 83]. It is observed that the E_{2g}¹ and A_{1g} mode peak characteristics are consistent with the presence of crystalline MoS₂, and the responses are similar for all the five different substrates, where the slight differences in Raman peak characteristics are expected when compared to the reports of Lee *et al.* [84] for variations due to MoS₂ thickness, with possibly further slight contributions from the underlying

substrate. The slightly broader peak seen for the MoS₂ on the a-Al₂O₃/sapphire substrate may also be partially due to a lower resolution setting at which this Raman spectra is obtained. While the crystalline order of the MoS₂ growth is similar in all cases, as evidenced by the Raman results, we do of course see differences in the interfacial structures and the growth thicknesses, for example, as seen in the cross-sectional HR-XTEM micrographs (see figure 1). The nucleation process on c-plane sapphire appears to generate an amorphous layer prior to the MoS₂ crystallite growth, likely due to the fewer nucleation sites available on c-plane sapphire compared to an amorphous surface. Our process is also very fast compared to many in the literature, and this likely contributes to the amorphous interlayer formation, until sufficient sites become available for crystallite MoS₂ growth to commence.

The amorphous nature of the SiO₂ on Si provides a wealth of nucleation sites for the crystallite growth of MoS₂ on this surface. Similarly, the amorphous nature of the ALD a-Al₂O₃ on sapphire or glass also offers a wealth of nucleation sites for MoS₂ growth. However, in this case, figure 1(e) showing the XTEM of MoS₂ on a-Al₂O₃/sapphire, which appears to be ~4–5 nm thick, exhibits some potentially mixed dark and light contrasting regions in the nominally a-Al₂O₃ layer under the MoS₂, which are possibly miscible regions with Mo and/or S incorporation. This is in contrast to the MoS₂ growth on the SiO₂/Si, figure 1(c), which is ~9–10 nm thick, and immiscible with SiO₂. The miscibility of the MoS₂ with the ALD a-Al₂O₃ is likely the reason why the polycrystalline layered MoS₂ is thinner on the a-Al₂O₃/sapphire substrate compared to the MoS₂ formation on the SiO₂/Si. Growth of the MoS₂ on ALD a-Al₂O₃/sapphire is likely delayed until a certain solubility level is reached prior to the commencement of layered growth. Looking again at figure 1(e), some partial crystallisation of regions of the nominally a-Al₂O₃ has taken place. This is likely due to the temperature of crystallisation of a-Al₂O₃ being lowered by the incorporation of Mo and/or S atoms. The MoS₂ growth directly on c-plane sapphire is also thinner than on the SiO₂/Si substrate, with a thickness of ~5–6 nm (excluding the out-of-plane features). This is similar to the 4–5 nm thickness of the MoS₂ growth on a-Al₂O₃/sapphire, and approximately half the thickness as observed on SiO₂/Si (~9–10 nm). The reduced MoS₂ crystallite growth thickness on the c-plane sapphire is likely contributed to by the formation of the amorphous interlayer. Some signs of possible diffusion of Mo and/or S in the c-plane sapphire bulk are observed in the HR-XTEM micrograph, but this is indeterminant. Regarding the observed out-of-plane MoS₂ features with respect to the horizontally-aligned layered MoS₂, these are particularly prominent on the c-plane sapphire surface, and relatively few are observed on the SiO₂/Si or a-Al₂O₃/sapphire substrates. Why these out-of-plane features are more common on the c-plane sapphire is unknown. One possibility is that the c-plane

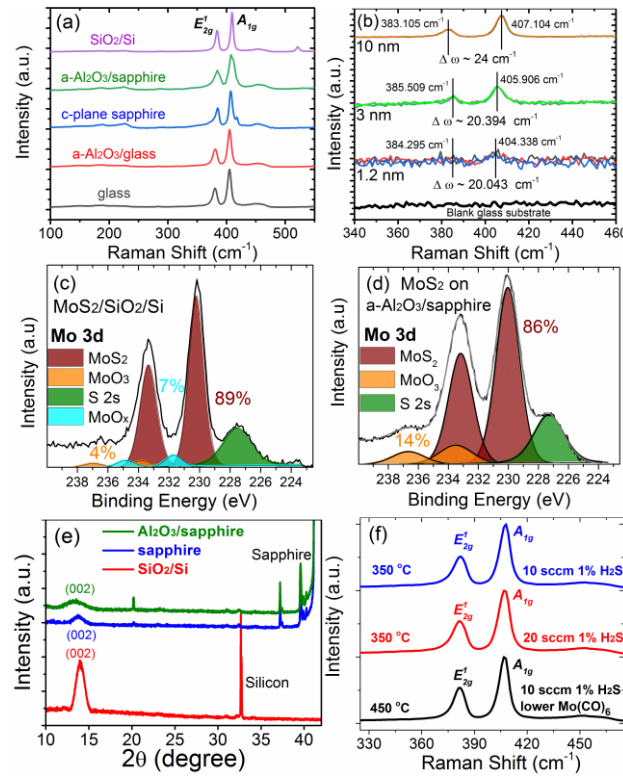


Figure 2. (a) Raman of MoS₂ (550 °C, 10 sccm 1% H₂S, 2.5 hours, nominally 10 nm) on all substrates under investigation. The Raman spectra show the characteristic MoS₂ peaks (E_{2g}^1 in-plane and A_{1g} out-of-plane modes). The small peak observed to the right of the A_{1g} mode for the MoS₂ on c-plane sapphire is related to this substrate. (b) Raman spectra of nominally 10 nm, 3 nm and 1.2 nm MoS₂ on glass, as well as the blank glass substrate. For each thickness, three representative spectra from three macroscale separated sites, are shown. Note that the noise observed from the glass substrate has an effect on the thinner MoS₂ Raman spectra. The positions of E_{2g}^1 mode and A_{1g} mode are indicated for each nominal thickness, but due to the significant substrate noise observed in the spectra for the nominally 1.2 nm MoS₂ film, the peak positions are statistically obtained from the 3 x 66 Raman microscale mapping at the three macroscale separated sites (note: they are not extracted solely from the plots shown here). The separation ($\Delta\omega$) between the two Raman modes are also indicated, which decreases with reducing MoS₂ thickness, in general agreement with the findings of Lee *et al.* [84]. Despite this correlation, we deduce that the thickness comparisons for peak separations underestimate our film thickness. (c,d) XPS of nominally 10 nm MoS₂ on SiO₂/Si and a-Al₂O₃/sapphire confirm that MoS₂ is formed with the presence of Mo-based sub-oxides and trioxide. (e) XRD of the normally 10 nm MoS₂ on SiO₂/Si, sapphire and a-Al₂O₃/sapphire substrates all show the MoS₂ (002) peak. (f) Raman spectra of the MoS₂ grown at 350 °C and 450 °C on SiO₂/Si substrates also show the characteristic MoS₂ peaks, confirming the formation of MoS₂ approximately at and below the BEOL thermal budget limit.

sapphire may be acting as a template for nucleation of the out-of-plane features.

Ex-situ XPS is performed and shown in figure 2(c) and 2(d) for nominally 10 nm MoS₂ on SiO₂/Si and a-Al₂O₃/sapphire, confirming the formation of MoS₂. The XPS also reveals the presence of MoO_x and MoO₃. Combined evidence exists confirming that the 2H phase of MoS₂ is formed instead of the 1T phase. Firstly, the 1T phase is not stable, and in vapour-phase growth processes, the formation of the 2H phase will generally be favoured. Secondly, for the 1T phase, the main E_{2g}^1 and A_{1g} Raman modes that are

characteristic of the 2H phase of MoS₂ are suppressed and broadened. Furthermore, when there is significant 1T phase present in a sample, there are additional "J" modes present in the Raman spectrum [85]. We do not observe these "J" modes, indicating that our phase is strongly 2H phase MoS₂. Thirdly, in terms of XPS of MoS₂, the fitted components for the 2H and 1T phase MoS₂ are at different positions in the Mo 3d core level spectra, and they have different line shapes [86]. The peak positions in the XPS are very close to the 2H phase, and the fitted peak shapes are symmetric, which is characteristic of the 2H phase, while the 1T phase MoS₂ has an asymmetric

peak shape owing to its metallic nature. Finally, the MoS₂ is very resistive (see section 3.2) and not metallic, so combining all of these findings, we can conclude that our MoS₂ is in the 2H phase.

Raman analysis on the nominally 10 nm, 3 nm and 1.2 nm MoS₂ on glass is shown in figure 2 (b), which gives a representative spectra from each of three macroscale separated sites, where a statistical microscale mapping is performed, which will be discussed later. Note that a similar thickness series on sapphire is also investigated, but this is unsuccessful due to the prominent Raman peak at ~416-418 cm⁻¹, which is due to the sapphire substrate (see figure S2, Supporting Information). Due to the combination of noise from the glass substrate, and the low intensity Raman peaks on the 1.2 nm film, the two Raman mode peaks are statistically estimated for this MoS₂ film from the large set of microscale mapping data over the three macroscale separated sites, and the peak values for this thin film are not determined solely from the spectra in figure 2(b) but from the statistical analysis shown later in figure 4(b). We focus our bulk measurements on the nominally 10 nm MoS₂. The separation ($\Delta\omega$) between the E_{2g} mode and A_{1g} mode are estimated to be: 24.0 cm⁻¹ for the nominally 10 nm MoS₂ (~15MLs), 20.4 cm⁻¹ for the 3 nm MoS₂ (~5MLs), and 20.0 cm⁻¹ for the 1.2 nm MoS₂ (~2MLs). Comparing these results from our low thermal budget polycrystalline grown MoS₂ to the single crystalline exfoliated MoS₂ flakes assessed in Ref [84], a similar trend is observed of decreasing $\Delta\omega$ with reducing nominal film thickness, confirming the reducing thickness sequence of the grown films, but before assessing the thickness interpretation it is beneficial to firstly estimate $\Delta\omega$ for the nominally 10 nm MoS₂ on all five substrates, as illustrated in figure 2 (a) and in figure 3 (b), where different Raman systems are used, for comparison. We obtain ~ 24.0 cm⁻¹ on glass, ~ 24.0 cm⁻¹ on a-Al₂O₃/glass, ~ 22.8 cm⁻¹ on c-plane sapphire, ~ 22.8 cm⁻¹ on a-Al₂O₃/sapphire, and ~ 22.8 cm⁻¹ on SiO₂/Si. While we know, for example, MoS₂ is ~9-10 nm (~14-15 ML) thick on the SiO₂/Si substrate from the HR-TEM in figure 1(c), the $\Delta\omega$ of ~ 22.8 cm⁻¹ corresponds to only ~ 2.8 ML in figure 2(b) of Ref [84]. This difference in peak separation, and therefore significant underestimation of the actual thickness, is likely contributed to by the dissimilar nature of our low thermal budget grown, small grain, polycrystalline MoS₂ in comparison to the high quality, large single crystal, exfoliated, MoS₂ flakes. In addition, Raman measurements carried out using different Raman kits with different settings could also contribute to variations in the results.

The thickness estimates from the $\Delta\omega$ of our films of different nominal thickness, also based on the work by Lee *et al.* [84], gives the following interpretations: The nominally 10 nm grown MoS₂ on glass gives ~ 24.0 cm⁻¹, which would correspond to ~ 4 ML (or ~ 2.6 nm); the nominally 3 nm grown

MoS₂ on glass gives ~ 20.4 cm⁻¹, which would correspond to ~ 1.8 ML (or ~ 1.2 nm); and the nominally 1.2 nm grown MoS₂ on glass gives ~ 20.0 cm⁻¹, which would correspond to ~ 1.5 ML (or ~ 1.0 nm). Given that the comparison to the work by Lee *et al.* underestimates our known thickness of ~ 9-10 nm (~14-15 ML) MoS₂ on SiO₂/Si, as deduced above, it is likely that these comparative thickness estimates are also underestimated.

Figure 2(e) shows the XRD of the MoS₂ deposited on SiO₂/Si, sapphire and a-Al₂O₃/sapphire substrates, which all show the MoS₂ (002) peak indicating the preferred c-axis orientation of the films. It is observed that the (002) peak is slightly weaker and broader on MoS₂ on a-Al₂O₃/sapphire than that on c-plane sapphire. This effect is likely a consequence of a combination of the reduced thickness growth of the layered MoS₂, and given the HR-TEM gives a thickness of ~4-5 nm, the XRD is likely also picking up the a-Al₂O₃ underneath, which is, in places, likely mixed with Mo and/or S. This potential mixing may also contribute to the formation of Mo-based oxides, for example, MoO₃, which has a peak at 12.5 degrees, and could contribute to the broadening of the (002) peak for the MoS₂ on a-Al₂O₃/sapphire [87].

Rapid growth depositions at 450 °C and 350 °C, which are approximately at and below the thermal budget limit for direct growth of semiconducting films at the BEOL, are also analysed. Raman spectra shown in figure 2(f) confirm the formation of MoS₂ grown by CVD with various precursor flows at 450 °C and 350 °C. These results suggest that the growth at lower temperatures may result in a more disordered film (figure S4 and table S1, Supporting Information), as it is expected from Ref [88].

To demonstrate repeatability of the CVD process and further support the HR-TEM thickness uniformity, microscale statistical mapping by Raman spectroscopy over macroscale separated sites (x3) on various nominal thicknesses of MoS₂ on various substrates are performed. Full details of Raman mapping experiments are included in the Supporting Information. Figure 3 and figure 4 show microscale mapping of the MoS₂ (statistically using 66 Raman measurements over an area of 15 µm x 15 µm), for three macroscale separated sites. In these mappings, the A_{1g} mode is demonstrated as an example. Representative Raman spectra from each microscale mapping set are also shown in figure 3(b), and the full 3 x 66 spectra from the microscale mapping are shown in figure 4(b). Note that all the Raman microscale statistical spectra (3 x 66 spectra across 15 µm x 15 µm at each macroscale separated site), for all the substrates investigated, are included in the figure S5 of the Supporting Information.

These MoS₂ films, as assessed in the Raman experiments detailed here, are grown in different deposition experiments under the same growth condition (550 °C, 10 sccm 1% H₂S,

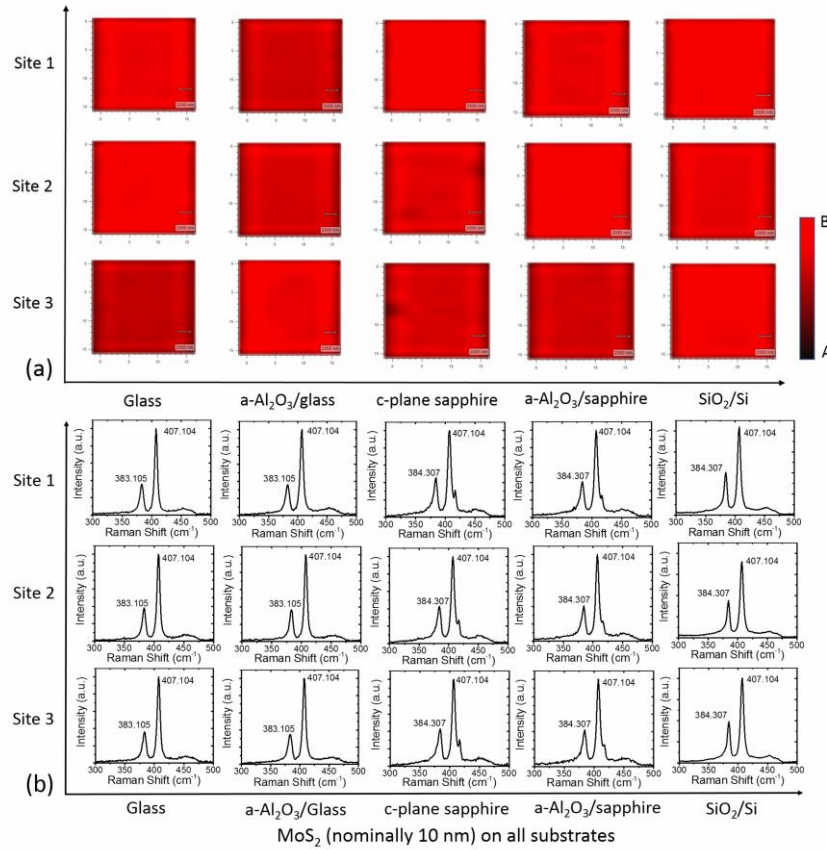


Figure 3. (a) Microscale mapping of MoS₂ (66 Raman measurements on an area of 15 μm x 15 μm) over three macroscale separated sites for nominally 10 nm MoS₂ on all substrates. Scale bar: 2000 nm. For these mappings, the A_{1g} peak intensity is demonstrated as an example. The colour on the microscale mapping images varies from black at intensity level A, to red at intensity level B, which corresponds to lowest and highest intensity, respectively. The intensity range (A to B) is set for the MoS₂ A_{1g} peak to be 0-7996 for glass, 0-6328 for a-Al₂O₃/glass, 0-3540 for c-plane sapphire, 0-4900 for a-Al₂O₃/c-plane sapphire, and 0-11450 for SiO₂/Si samples; and (b) The representative Raman spectra for each site.

2.2 Torr) for different process times, and for different thicknesses. The extensive sets of Raman mappings confirm, in a statistical manner, that MoS₂ is formed in all these depositions, across five different substrates, and across three different thicknesses. Furthermore, the uniformity of the MoS₂, indicated by the macroscale separated sites that underwent microscale mapping, is excellent, with very similar Raman spectra obtained from the extensive number of statistical spectra per site, and across three macroscale separated sites.

The very dark red colour on the thinnest MoS₂ of nominally 1.2 nm thickness in figure 4(a) is attributed to the very weak A_{1g} mode that is not very well defined. Moreover, subtracting the baseline for this sample is challenging. The weak and noisy Raman spectra for the nominally 1.2 nm film is affected by the underlying glass substrate (see figure 2(b) for the equivalent Raman spectra on a blank glass substrate). The E_{12g} and A_{1g} modes on the 1.2 nm MoS₂, although weak, are still

visible and statistically detectable from the large set of Raman mapping data. Hence, in order to define the 1.2 nm Raman peaks more accurately, a statistical analysis is performed from the large set of Raman mapping data and the two Raman peaks are estimated on this MoS₂ thin film (see figure 4 (b) and the caption with the mean values of the two Raman peaks, which also includes the standard deviation values). These results indicate that MoS₂ is formed uniformly over large areas, with a high repeatability of the CVD growth across a large set of depositions.

Furthermore, AFM analysis is performed on MoS₂ on SiO₂/Si, c-plane sapphire, a-Al₂O₃/sapphire, glass, and a-Al₂O₃/glass substrates as shown in figure 5. The AFM scans are taken at numerous sites, which all show smooth MoS₂ surfaces with low roughness values. The roughness for MoS₂ on a-Al₂O₃/glass is the highest among all the samples, but comparing the AFM of the blank a-Al₂O₃/glass (see figure 5 (h)) with the AFM of the MoS₂ on this substrate, a similar

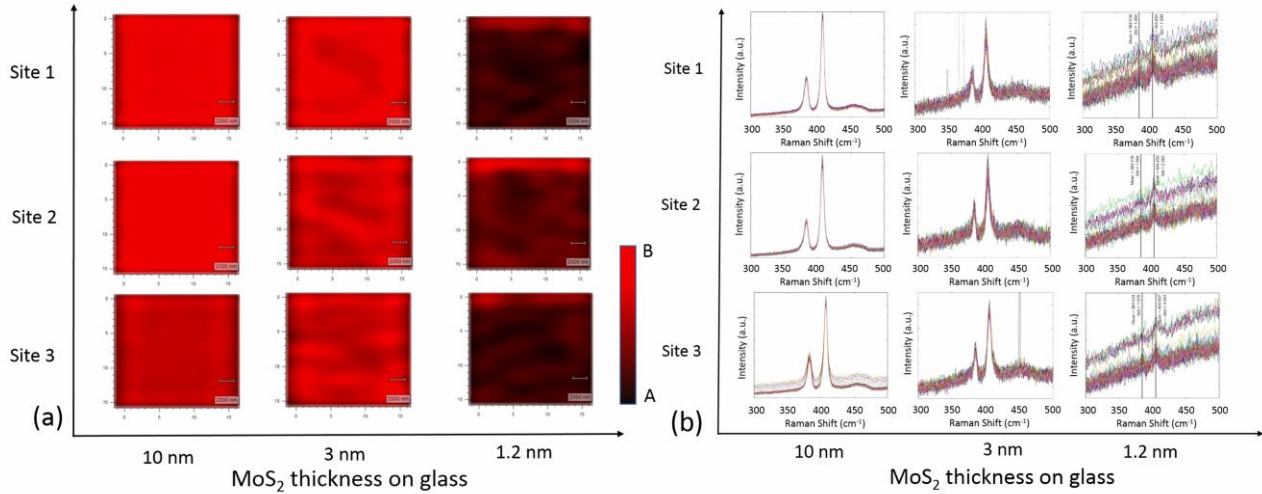


Figure 4. (a) Microscale mapping of MoS₂ (66 Raman measurements on an area of 15 μm x 15 μm) over three macroscale separated sites for nominally 10 nm, 3 nm and 1.2 nm MoS₂ on glass. Scale bar: 2000 nm. For these mappings, the MoS₂ A_{1g} peak intensity is demonstrated as an example. The colour on the microscale mapping images varies from black at intensity level A, to red at intensity level B, which corresponds to lowest and highest intensity, respectively. The intensity range (A to B) is set for the MoS₂ A_{1g} peak to be, 0-7996 for 10 nm, 0-760 for 3 nm, and 1100-1600 (inflated intensity range due to the substrate noise effect) for 1.2 nm, samples; and (b) The 3 x 66 Raman spectra that gives the mapping plots in (a) for each nominal thickness. Mean (M) and standard deviation (SD) values in the 1.2 nm graphs of (b) are presented here for clarity: Site 1, M/SD [E_{2g}] = 384.034/1.964, [A_{1g}] = 403.654/1.580; Site 2, M/SD [E_{2g}] = 384.416/1.894, [A_{1g}] = 404.453/2.363; and Site 3, M/SD [E_{2g}] = 384.434/1.979, [A_{1g}] = 404.907/3.063.

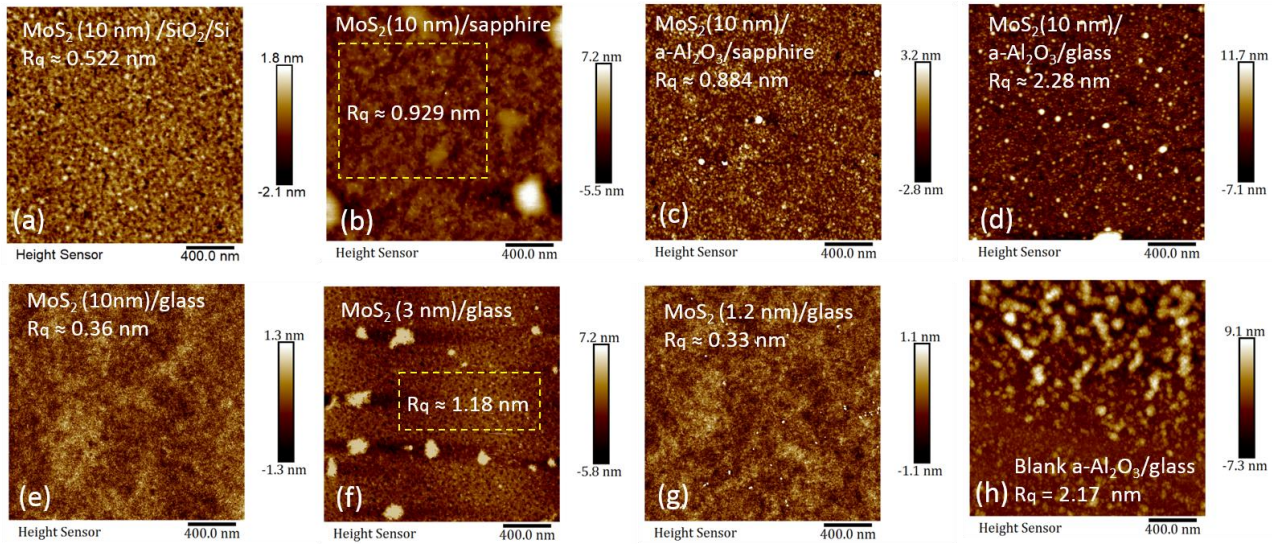


Figure 5. AFM of MoS₂ (nominally 10 nm) on (a) SiO₂/Si, (b) c-plane sapphire, (c) a-Al₂O₃/sapphire, (d) a-Al₂O₃/glass and (e) glass substrates. Thinner MoS₂ of nominally 3 nm and 1.2 nm are also shown in (f) and (g), respectively. (h) AFM of blank a-Al₂O₃/glass, which indicates that the roughness shown in (d) is an artefact of the underlying substrate.

roughness value is observed, therefore it is concluded that the roughness observed for the MoS₂/a-Al₂O₃/glass sample is an artefact of the underlying substrate. AFM analysis for thinner MoS₂ is also performed, giving low roughness values, and are also shown in figure 5 (f) and (g) for ~3 nm and ~1.2 nm MoS₂ on glass, respectively. The AFM results provide further evidence of the MoS₂ film uniformity and continuity. Finally

and importantly, when these results are combined with the Raman/XPS/XRD, it is conclusive that our MoS₂ grains are in the 2H phase with good crystalline order, and that we have uniform and continuous thicknesses, with a high degree of repeatability.

Table 1. Room temperature Hall/4P results using a high-resistance unit on Van der Pauw structured MoS₂ (350–550 °C, 10 sccm 1% H₂S, 2.5 hours).^a Results for the patterned VdP structures of MoS₂ (etched and metal-contacted) are also shown.

Growth Condition	ρ_s [G Ω /sq.]	ρ [k Ω cm]	Carrier type	n_s [cm ⁻²]	n [cm ⁻³]	μ_H [cm ² V ⁻¹ s ⁻¹]
550 °C sapphire	3.561	1.959	<i>n</i> -type	1.05×10^8	1.91×10^{14}	16.72
550 °C a-Al ₂ O ₃ /sapphire	5.768	2.596	<i>n</i> -type	3.28×10^8	7.29×10^{14}	3.30
450 °C a-Al ₂ O ₃ /sapphire	2.351	1.411	<i>n</i> -type	1.09×10^9	1.82×10^{15}	2.44
350 °C a-Al ₂ O ₃ /sapphire	3.483	2.961	<i>p</i> -type	3.69×10^9	4.34×10^{15}	0.49
550 °C (patterned) sapphire	4.433	2.438	<i>p</i> -type	2.84×10^8	5.16×10^{14}	4.96
550 °C (patterned) a-Al ₂ O ₃ /sapphire	7.356	3.310	<i>p</i> -type	3.58×10^8	7.96×10^{14}	2.37

^a The resistivity and carrier concentration are calculated from the obtained sheet values based on the estimated thickness from HR-XTEM. Carrier concentration (n) is calculated using $n = n_s/t$ [cm⁻³] and resistivity (ρ) is calculated using $\rho = \rho_s \times t$ [Ω cm], where n_s is the sheet carrier concentration [cm⁻²], ρ_s is the sheet resistivity in [Ω/square] or [Ω/sq.], and t is the thickness [cm]. Hall mobility is determined by $\mu_H = 1/(q \times n_s \times \rho_s)$ [cm² V⁻¹ s⁻¹], assuming a Hall factor of 1 in all cases. The signal-to-noise ratio of the Hall-effect on the 550 °C-grown MoS₂ on a-Al₂O₃/sapphire – which has a similar resistivity to the film on sapphire – is not ideal. However, corroboration is provided by c-TLM resistor and field-effect transistor analysis for ρ , n , and μ_H in the Supporting Information.

3.2 Hall-effect Properties, 4P Resistivity and Logic

Hall/4P/2P measurements using a high-resistance unit are carried out in ambient at RT on MoS₂ using a 1 cm × 1 cm VdP structure (figure S6 (a), Supporting Information) [89]. Excellent ohmic behaviour is achieved although the 2P/4P resistance is very high (2P resistance ~16 GΩ in figure S6 (b), Supporting Information), both with/without a high contact resistance. The Hall-effect measurements are all obtained from a DC magnetic field (± 1.7 T, i.e. 1.7×10^4 G). A sufficiently long hold time (up to 420 seconds) is applied before each measurement in order to stabilise current before measuring the total voltages in Hall/4P. Moreover, a sufficient average count (up to 500) of measured results is used. Therefore, reasonably reliable results are obtained with approximate average signal-to-noise ratios of ~11:1 for the Hall-effect measurements and ~374:1 for the 4P resistance/resistivity measurements. Table 1 gives a summary of Hall/4P results. More information on the Hall/4P/2P measurements are provided in the Supporting Information. The MoS₂ deposited at all temperatures exhibits very high resistivity values (1.4–3.3 kΩ cm). The 550 °C-grown MoS₂ films are *n*-type with very low carrier concentrations on the order of 10^{14} cm⁻³ and electron mobility in the range of 3.3–16.7 cm² V⁻¹ s⁻¹. The carrier concentration of the MoS₂ grown at 450 °C and 350 °C is on the order of 10^{15} cm⁻³. The 450 °C-grown film is also *n*-type with a mobility of 2.4 cm² V⁻¹ s⁻¹. A

possible source of the *n*-type behaviour is the density of sulfur vacancies [90]. The MoS₂ grown at 350 °C is found to be *p*-type by Hall-effect analysis with a mobility of 0.5 cm² V⁻¹ s⁻¹. Sulfur vacancies are susceptible to oxidation in atmosphere leading to increasing MoS_xO_{3-x} cluster growth that give *p*-type doping [82], and therefore an *n*-type MoS₂ film under appropriate oxidation conditions could be gradually transformed to *p*-type.

The very low carrier concentrations determined from the Hall-effect analysis for all growth temperatures (10^{14} – 10^{15} cm⁻³) is consistent with defects in the MoS₂ structure resulting in states in the MoS₂ energy gap. Such energy gap states are predicted from First Principles calculations [91], and capture free carriers provided by any unintentional doping in the MoS₂. It is noteworthy that this shares a similarity with the early work on polycrystalline silicon, where dopant saturation of grain boundary defects was required to achieve controlled semiconductor or pseudo-metallic behaviour [92, 93].

It is observed that the CVD-grown MoS₂ can be gradually switched from *n*-type to *p*-type by repeated electrical or electromagnetic measurements. Furthermore, it is also observed that the net carrier type is switched to *p*-type after VdP patterning (figure S6 (c), Supporting Information), with similar carrier concentrations compared to the non-patterned

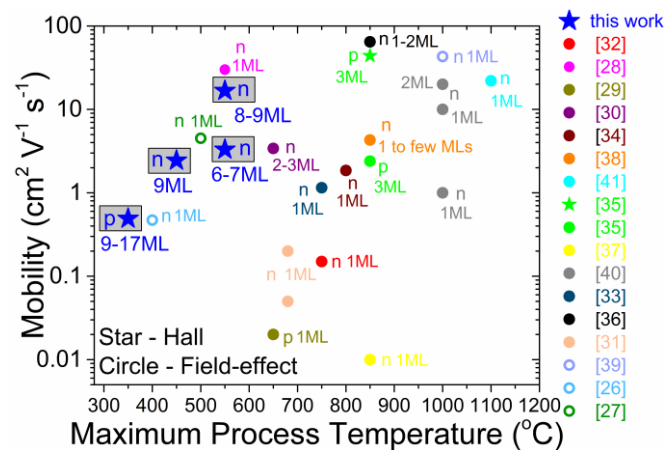


Figure 6. Mobility values of CVD-grown MoS₂ in this work (blue stars) and those reported in the literature (table 2). Stars and circles represent Hall mobility and field-effect mobility, respectively. The carrier type and number of monolayers (ML) for each maximum process temperature are also indicated. The blue star symbols (Hall mobility of MoS₂ grown at 350–550 °C, 10 sccm 1% H₂S, 2.5 hours) from this work span the lower left part of the temperature x-axis, which is approximately at and below the desired BEOL thermal budget limit for CMOS process compatibility.

MoS₂ (table 1). Due to the low carrier concentrations, only a relatively small movement in the MoS₂ Fermi level is required to switch the MoS₂ from *n*-type to *p*-type. A possible source of the slightly modified Fermi level position is the resist coating and removal during the patterning process. In the case of repeated electrical measurements, the shift from *n*-type to *p*-type behaviour is consistent with progressive oxygen reaction with the MoS₂, driven by the power dissipation in the MoS₂ thin film combined with the fact that the top MoS₂ surface is exposed to ambient conditions [82, 94]. The presence of MoO_x in the MoS₂ layer is evident in the XPS results (see figure 2(c,d)).

Moreover, the measured current through the patterned-VdP structures of MoS₂ over the bias range -10 V to +10 V demonstrates an activation energy of ~215–216 meV (figure S7, Supporting Information), consistent with the reported acceptor energy of 214 meV above the valence band maximum which is attributed to MoS_xO_{3-x} *p*-type dopant clusters [82].

A comparison of the Hall mobility values determined in this work with the field-effect and Hall mobility values from CVD-MoS₂ literature [26-41] is shown in figure 6. It is noted that the Hall mobility, which is related to the longitudinal (in-plane) electric field, is different to the field-effect mobility, which is affected by both the longitudinal and transverse, out-of-plane, electric fields (their correlation is discussed in the Supporting Information). The mobility values in figure 6 are plotted versus the maximum process temperature experienced by the MoS₂ samples, either during growth or during a pre/post deposition annealing. The full data associated with the comparative published works are included in table 2. There are also a number of literature reports on MoS₂ grown by ALD

at relatively low temperatures [43-51], either with or without a high-temperature post-deposition annealing (as detailed in table S3, Supporting Information), but very few report electrical results making comparison difficult. As observed in figure 6, there is no clear trend in the mobility variation of the CVD-grown MoS₂ with process temperature, despite the wide variety of growth conditions (CVD setup, precursors, temperatures, substrates and annealing), and a corresponding range of grain sizes from ~10 nm to ~1 μm. Importantly, in the majority of the literature reports, the CVD/ALD MoS₂ is processed beyond the BEOL thermal budget limit, making those materials unsuitable for 3D BEOL heterogeneous integration applications.

The values of resistivity, carrier concentration and mobility determined from the Hall analysis are consistent with results obtained from micro-scale c-TLM resistor measurements and back-gated MOSFETs. These comparisons are obtained on the 550 °C-grown MoS₂ (~10 nm) on SiO₂/Si (see figure S8, figure S9 and related notes, Supporting Information). In relation to the back-gated MoS₂ MOSFETs, the current levels are in good agreement with the values of carrier concentration and mobility obtained from the Hall analysis. However, the MoS₂ MOSFETs exhibit only a limited modulation of the drain-source current with the back-gate voltage, consistent with the small grain size observed in HR-XTEM and plan-view TEM analysis, and theoretical prediction that MoS₂ defects create states through the MoS₂ energy gap. It should be noted that transport properties of MoS₂ films nominally 5 nm (~7-8 ML) and less are also assessed in this work, where possible, by 2-point/4-point/Hall-effect, c-TLM and back-gated MOSFET analysis, but the small grain films are found to be highly resistive, which increases prohibitively with reducing film thickness. Furthermore, device processing by

Table 2. Growth details from the various literature reports of CVD-grown MoS₂, as compared in figure 6 for mobility and BEOL compatibility. The first column “Method/*T*” refers to the method (CVD/MOCVD) and maximum process temperature (*T*) experienced by the MoS₂, either during growth or during a pre/post deposition annealing.

Method/ <i>T</i>	Precursors/Substrates /Annealing	Comments	Ref.
CVD 350-550 °C	Mo(CO) ₆ (carried by N ₂) + H ₂ S (carried by Ar), 2.5 hours, on SiO ₂ /Si, sapphire or a-Al ₂ O ₃ /sapphire.	Measured at RT/ambient, Hall on MoS ₂ on sapphire or a-Al ₂ O ₃ /sapphire	this work
MOCVD 400 °C	Mo(CO) ₆ + H ₂ S in Ar or H ₂ flow, on SiO ₂ /Si, 9 hours for full monolayer coverage.	Measured at RT	Kim <i>et al.</i> [26]
CVD 500 °C	Tellurium-assisted CVD MoO ₃ + sulfur in Ar, on SiO ₂ /Si, 15 minutes.	FET annealed in vacuum for 2 hours at 120 °C	Gong <i>et al.</i> [27]
MOCVD 550 °C	Mo(CO) ₆ + (C ₂ H ₅) ₂ S + H ₂ carried by Ar, on SiO ₂ /Si, 26 hours for 1 monolayer.	30 cm ² V ⁻¹ s ⁻¹ at RT/ambient, 114 cm ² V ⁻¹ s ⁻¹ at 99 K	Kang <i>et al.</i> [28]
CVD 650 °C	MoO ₃ powder + sulfur powder in N ₂ flow, 15 minutes, on SiO ₂ /Si.	FET exhibited <i>n</i> -type, reported FE mobility of holes	Lee <i>et al.</i> [29]
CVD 650 °C	MoO ₃ powder + sulfur powder in Ar flow, 30 minutes, on SiO ₂ /Si.	Measured at RT/ambient	Chen <i>et al.</i> [30]
CVD 680 °C	MoO ₃ + sulfur in Ar, on SiO ₂ /Si, 5-30 minutes.	Measured at RT	Zheng <i>et al.</i> [31]
CVD 750 °C	Mo(CO) ₆ + H ₂ S (no carrier gas), growth at 350 °C, ~12 hours, SiO ₂ /Si substrate that is pre-growth annealed in high-vacuum at 750 °C for 140 minutes.	Measured at RT/ambient	Mun <i>et al.</i> [32]
CVD 750 °C	Liquid-phase exfoliated MoO ₃ + sulfur in Ar flow, 20 minutes, on SiO ₂ /Si, post-sulfurisation anneal in Ar at 750 °C for 20 minutes.	Measured at RT/vacuum (device annealed in vacuum at 400 K for 140 minutes before electrical measurements)	O'Brien <i>et al.</i> [33]
CVD 800 °C	MoO ₃ powder + sulfur powder under Ar flow, 20 minutes, on ALD-Al ₂ O ₃ /Si.	Measured at RT, < 5 × 10 ⁻⁵ Torr	Bergeron <i>et al.</i> [34]
CVD 350-850 °C	Mo(CO) ₆ powder (vaporised) + H ₂ S, carrier gas Ar and/or H ₂ , on SiO ₂ /Si, sapphire or fused quartz, MoS ₂ achieved at > 350 °C, 3 monolayers at 850 °C for 60 seconds.	850 °C-grown MoS ₂ for electrical analysis, film transferred to SiO ₂ /Si for FET, FET/Hall on MoS ₂ on SiO ₂ /Si	Kumar <i>et al.</i> [35]
CVD 850 °C	MoO ₃ + sulfur under Ar flow, on SiO ₂ /Si or ZrO ₂ /Si, 30 minutes	FET studied on both substrates. Higher crystalline quality on ZrO ₂ than on SiO ₂ . Best mobility on MoS ₂ /ZrO ₂ long channel FET.	Liu <i>et al.</i> [36]
CVD 850 °C	MoCl ₅ powder + sulfur powder in Ar flow, ~10 minutes, on SiO ₂ /Si, sapphire or graphite.	Film transferred from sapphire to SiO ₂ /Si for FET, measured at RT/ambient	Yu <i>et al.</i> [37]
CVD 850 °C	MoO ₃ films + sulfur under N ₂ flow, ~10-15 minutes, on SiO ₂ /Si.	Measured at RT/vacuum (10 ⁻⁵ Torr)	Najmaei <i>et al.</i> [38]
CVD 1000 °C	MoO ₃ + sulfur in Ar, on sapphire, growth at 700 °C (10 minutes), and substrate is pre-growth annealed for 1 hour at 1000 °C in air.	Film transferred to SiO ₂ /Si for FET. Several anneal (130-350 °C) steps applied during FET fabrication, measured at RT in vacuum.	Dumcenco <i>et al.</i> [39]
MOCVD 1000 °C	Mo(CO) ₆ + H ₂ S carried by N ₂ & H ₂ , on sapphire, growth at 700-900 °C, 15-20 minutes, post-growth annealing in N ₂ /H ₂ S at 1000 °C.	Film transferred from sapphire to SiO ₂ /Si for FET	Chiappe <i>et al.</i> [40]
MOCVD 1100 °C	(C ₂ H ₅) ₂ S carried by Ar + H ₂ flow through Na ₂ MoO ₄ coated sapphire or SiO ₂ /Si substrate, growth at 850 °C, 20 minutes, sapphire is pre-growth annealed at 1100 °C for 1 hour.	Film transferred from sapphire to SiO ₂ /Si for FET, measured at RT/vacuum (2 × 10 ⁻⁷ mbar)	Cun <i>et al.</i> [41]

lithography and lift-off, are challenging for 2D materials, particularly for the nominally thinner 1.2 nm and 3 nm MoS₂ films. Future methods of functionalisation for lateral transport within the BEOL thermal budget limit is needed, as well as

compatible processing developments for 2D materials. Potential routes to enhance lateral transport include laser annealing [15], electron wind force annealing [42], doping/surface functionalisation [95-98] and 2D stacking

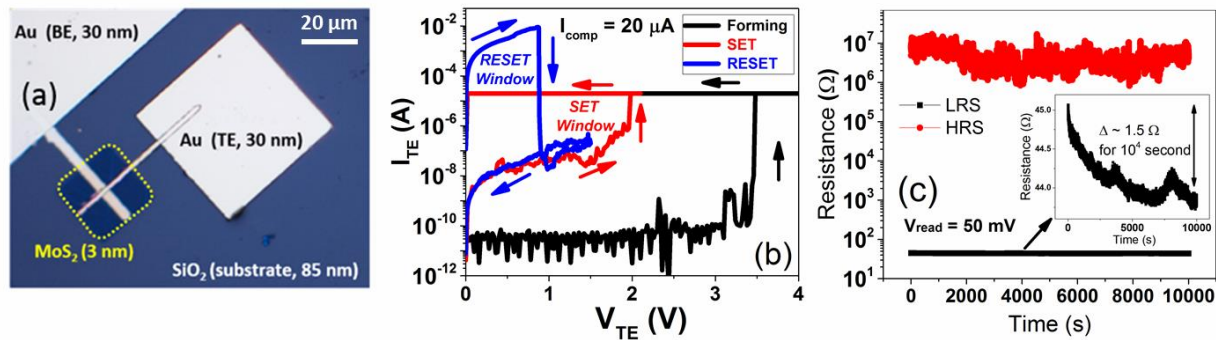


Figure 7. (a) The Au/MoS₂/Au memristor device, where the MoS₂ is nominally 3 nm thick (550 °C, 10 sccm 1% H₂S, 0.75 hours). During the DC measurements in ambient, the bottom electrode (BE) is tied to common ground, whereas the top electrode (TE) is used as the sweeping terminal. This device exhibits (b) memristive switching with distinct forming (black), RESET (blue) and SET (red) characteristics and (c) a stable memory window 10⁵ between the high and low resistive states with a retention time of > 10⁴ seconds.

[99]. In the choices of MoS₂ film thickness for memristors and sensors, which will be discussed in section 3.3 and section 3.4, we target the thinnest films as possible for (1) memristors to reduce power requirements, and (2) for sensors, which are surface sensitive devices, and hence the surface to volume ratio is maximised as far as feasibly possible.

3.3 Memristors for Non-volatile Resistive Memory

Although the preliminary reports on memristors in both lateral [53, 54] and vertical [55–59] structures are promising, the associated benefits of having only a monolayer of active layer sandwiched between two metal electrodes for reduced operational voltages, and hence low energy (power) consumption remains elusive. In a previous work on monolayer MoS₂ [59], the role of formation and migration of sulfur vacancies in understanding the microscopic mechanism of resistive switching was explored, suggesting that it is beneficial to engineer defects into the film during the growth process in order to tune device performance. While the presence of defects and grain boundaries in CVD-grown polycrystalline MoS₂, as opposed to crystalline MoS₂, can be detrimental for the modulation of lateral (in-plane) transport in FETs, vertical (out-of-plane) transport resistive switching behaviour is observed in crystalline MoS₂ structures [55, 59]. The incorporation of oxygen into MoS₂ can improve the robustness of the memristive behaviour [100].

In this work, memristive switching of low-thermal-budget, BEOL-compatible MoS₂ (~3 nm, 550 °C, 10 sccm 1% H₂S, 0.75 hours) is examined using structures described in section 2.3 and shown in figure 7(a). Initially the device demonstrates very high resistivity, necessitating a forming step to create a conducting filament, which typically occurs at ~3.5 V (figure 7(b)). The optimum compliance current (I_{comp}) for the forming step and subsequent SET cycles is around 10–50 μ A; below this value the memory window shrinks considerably, and

above this value the device may experience permanent breakdown (inability to RESET again). However, during the RESET process, it is essential to remove the current compliance and restrict the voltage sweep below the set voltage. Both the SET and RESET cycle demonstrate abrupt, bi-stable, unipolar switching with a large memory window of nearly 5 decades and $V_{set} > V_{reset}$ typically around 2 ± 0.4 V and 0.9 ± 0.2 V, respectively. Here, it is instructive to compare the SET and RESET voltages of our devices with previous reports that benefit from being single-crystalline monolayer MoS₂ grown at higher temperature > 850 °C [55, 59, 101], which are not BEOL compatible and exhibiting typical SET voltages of 3.5–4 V and RESET voltages of 1.5–1.8 V. Moreover, the devices in this work have an abrupt transition, whereas in the crystalline MoS₂ material, the RESET process is gradual [59]. As evident in this work, despite a larger thickness (~3 \times) of the film, the incorporation of grain boundaries and sulfur defects considerably reduces the operational voltages, thus reducing the power/energy consumption of the device. However, it is important to note that a large amount of current (10 mA at 1 V), and hence power density (10 W cm⁻²), is still required to RESET the device; pointing to the importance of Joule heating to disrupt/contract the conducting filament. These observations clearly indicate that the rupture/restoration of the conducting pathway is due to a thermochemical (TCM) memory assisted mechanism [102, 103]. As shown in the previous work [59], the creation and diffusion of sulfur vacancies leading to conductive states in the bandgap can reasonably explain the microscopic origins of such current carrying pathways. Hence, from this perspective it is possible to understand the lowering of operational voltages in our material. Stoichiometric defects lower the energy barrier and hence the electric field required to ‘extract’ sulfur ions from lattice sites and create vacancies, which lead to the SET process. Additionally, the presence of grain boundaries in the material aids the diffusion of sulfur

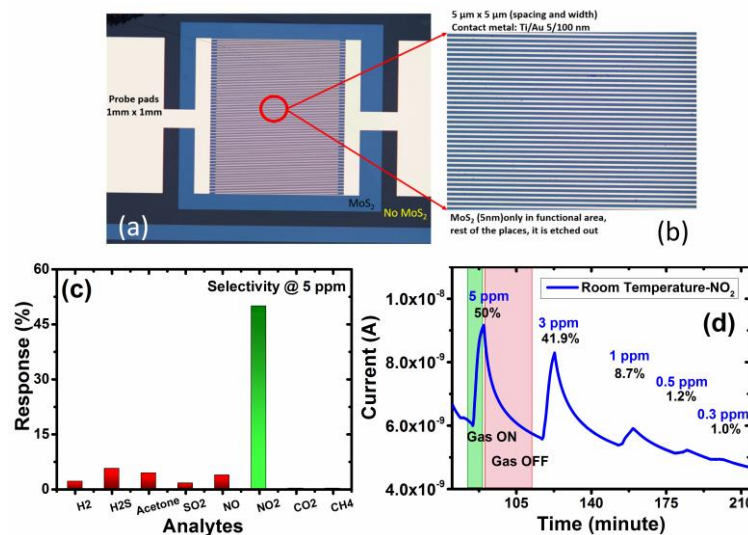


Figure 8. (a) Optical image depicting the structure of interdigitated electrodes with underlying MoS₂ (550 °C, 10 sccm 1% H₂S, 1.25 hours) thin film of ~5 nm with a magnified area shown in (b). (c) Histogram depicting selectivity of NO₂ against other interfering gases at 5 ppm (y-axis: Modulus of Response (%)). (d) Transient response/recovery plot of NO₂ in the concentration range of 0.3 ppm to 5 ppm at room temperature. A DC bias of 5 V was provided during the measurement.

vacancies due to Joule heating in the RESET cycle, i.e. the RESET process is facilitated by the Joule heating induced 'repair' of these vacancy sites.

Next, the retention time of these devices is examined at a read bias of 50 mV (figure 7(c)). The average value of resistance of the low resistance state (LRS) and high resistance state (HRS) is ~45 (±1.5) Ω and ~5 (±3) MΩ, respectively. The Au/MoS₂/Au structures exhibit non-volatile resistive memory for over 10⁴ seconds with a memory window of close to 5 decades. The retention time and memory window (marginal improvement), are seen to be reasonably unaffected by the higher number of sulfur defects and grain boundaries in the MoS₂ films of this work. Therefore, while we do not claim that this BEOL-compatible MoS₂ memristor competes with the performance of unconstrained state-of-the-art equivalent memory devices, we have achieved the objective of demonstrating BEOL-compatible MoS₂ memory functionality [17, 18], with reduced energy consumption.

3.4 Sensors for Selective NO₂ Gas Sensing Applications

MoS₂ is inherently well-suited for gas sensing applications as it can provide significant sulfur-vacancies on the MoS₂ basal plane that act as active adsorption sites for target analytes [104], and can also be further modified using substitutional doping [105, 106]. Furthermore, the presence of defects stimulates the sensing performance by introducing additional gap states at the Fermi level [107]. In this work, the ~5 nm polycrystalline CVD-grown MoS₂ at 550 °C (10 sccm 1% H₂S, 1.25 hours) is employed as a sensing material for chemiresistive devices (see figure 8 (a) and (b)). Initially, the

sensor is stabilised in the presence of dry air before exposing it to different analytes. Subsequently, it is subjected to a pool of interfering reducing gases such as H₂, H₂S, Acetone, SO₂, NO, NO₂, CO₂, and CH₄ at RT. Among these, a remarkable selectivity towards NO₂ is observed (figure 8(c)). It can be attributed to the strong binding of NO₂ to MoS₂ with large adsorption energies compared to other analytes, as supported by the theoretical and experimental study by Zhao *et al.* [108]. We obtain a dynamic current response (figure 8(d)) of the device for NO₂ concentrations of 0.3–5 ppm. Due to the independently-observed *p*-type characteristic of the MoS₂ receptor film, as seen in all cases after device processing (and reported in section 3.2), the absolute current value increases with purging of an oxidising gas like NO₂ due to its electron extracting characteristic.

We also obtain the response (in %) of the device from the dynamic current curve to determine the static response vs NO₂ concentration, as shown in figure 9(a), where the sensor response (%) is given by equation (1),

$$R(\%) = \frac{I_g - I_a}{I_a} \times 100 \quad (1)$$

where I_g and I_a are the electrical currents measured in the presence of target analyte and dry air, respectively. The response signal decreases stepwise with decreases in NO₂ concentration while it is swept from 5 ppm to 0.3 ppm NO₂. The sensor could precisely detect to as low as 0.3 ppm with a clear R response magnitude of 1% while responding significantly ($R \approx 50\%$) towards 5 ppm NO₂. The response vs NO₂ concentration plot is also fitted to an empirical linear

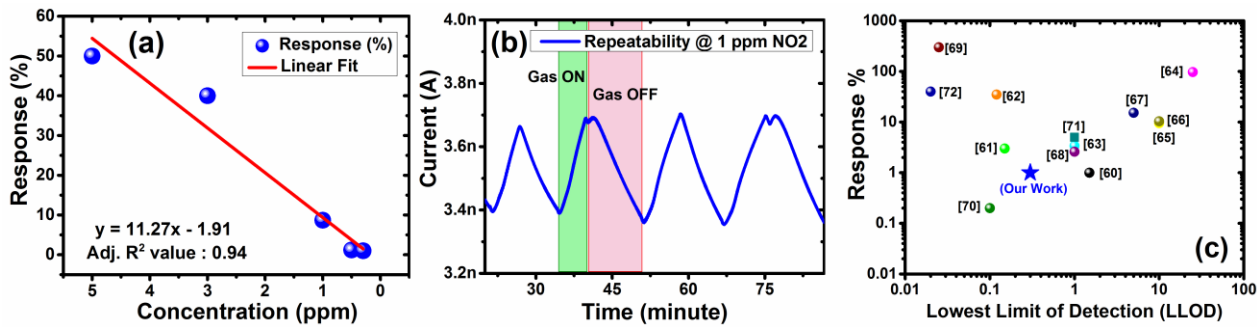


Figure 9. (a) Linearly fitted response (%) versus NO₂ concentration plot. (b) Repeatability cycles of 1 ppm NO₂ at room temperature. (c) Benchmarking of MoS₂ thin-film-based sensor with existing CVD-grown MoS₂-based NO₂ sensors operated at room temperature. Our work is included (blue star). The room temperature recovery of our sensor is remarkable compared to other works in the literature that report higher responses or better LLOD, which suffer from the drawback of sluggish or no recovery at room temperature.

equation ($y = 11.27x - 1.91$). The high value of coefficient of correlation (0.94) between experimental and fitted data confirms the linearity of the sensor which ensures reliable operation in the range of 0.3 ppm to 5 ppm NO₂, as evident in figure 9(a). The sensitivity derived from this linearly-fitted response versus concentration plot is found to be 11% / ppm. Figure 9(b) shows very repeatable and stable sensing behaviour when the sensor is exposed to four consecutive on-off pulses of 1 ppm NO₂ (with NO₂ on for 223 seconds and off with synthetic air purge for 525 seconds constituting one cycle).

Another important factor is the response time and recovery time of the sensor. It takes an average of 3–4 minutes for the sensor to respond to all the concentrations of NO₂ while showing the least time towards 5 ppm NO₂. On the other hand, it takes almost 15 minutes to recover back to the baseline signal for 5 ppm NO₂ and less than 3 minutes for 0.3 ppm NO₂. This sluggish response/recovery behaviour is obviously owing to the typical RT operation of the sensor. Nevertheless, the complete recovery at RT without providing any external stimulus, is exemplary. We have seen from the recent literature reports that the strong affinity of NO₂ towards MoS₂ makes it difficult to recover at lower temperatures [62, 66, 67, 75]. For instance, Agrawal *et al.* [66] demonstrated an edge-enriched MoS₂-based NO₂ sensor prepared via modified atmospheric pressure CVD. It could detect as low as 10 ppm NO₂ with 10.36% response magnitude without recovering at RT. Therefore, they utilised UV as an external energy source for the recovery of the sensor [66]. Another report employed a CVD-grown MoS₂-based chemiresistive device for sub-ppm NO₂ detection at RT but again used thermal annealing at 100 °C for the complete recovery to its original baseline [62].

Therefore, the sub-ppm detection achieved here along with the remarkable recovery at RT is extraordinary and competes well with the existing reports in the literature. Figure 9(c) (full

data detailed in table S4, Supporting Information) compares our sensor's performance with some of the existing RT reports on CVD-grown MoS₂-based NO₂ sensors in the literature. It should be noted from figure 9(c), the reports in [61, 62, 69, 70, 72], while reporting higher percentage responses, or better lowest limit of detection (LLOD), than what we report here, their devices suffer from the drawback of sluggish or no recovery at RT and require external sources such as UV, red light illumination, thermal annealing, etc. to recover the sensor to its original baseline value (as detailed in table S4, Supporting Information). To deploy such sensors in the field, it would require additional circuitry, cost and most importantly, energy consumption. Moreover, the shelf life of the sensor would degrade over time due to poor recovery. Hence, the remarkable recovery of our sensor at RT without any additional circuitry, cost or energy input makes it amenable to real-time applications, thus providing an improved shelf life sensor with a reduced carbon footprint. These features distinguish the performance of our sensor from the reported works (on CVD-grown MoS₂-based sensors) in the literature.

To understand the underlying mechanism behind the remarkable recovery, we would like to quote the presence of MoO₃ in trace levels onto the surface of MoS₂ films as corroborated by XPS and Raman signatures in this study. This has been attributed to the presence of sulfur vacancies. These defects are known to tailor the gas sensing properties by enhancing the active sites of adsorption [109]. Hence, it is reasonable to assume that the presence of the MoO₃ onto the surface MoS₂ aid in complete recovery of our sensor without any external stimulus. During the recovery process, the oxygen is chemisorbed on the surface of the MoO₃ leading to desorption of NO₂ ($\text{NO}_2^{\text{(ads)}} + \text{O}^{\text{(ads)}} \rightarrow \text{NO}_2^{\text{(gas)}} + 2\text{O}^{\text{(ads)}}$) which is otherwise difficult on pristine MoS₂. This is also observed by Kumar *et al.* [110], who investigated hybrid of MoS₂ and MoO₃ for detection of NO₂ and reported excellent

recovery at room temperature. This has been explained based on the synergistic effect of hybrid and oxygen chemisorption on MoO₃ during the process of recovery. In fact, the hybrids of metal oxides and dichalcogenides in general have shown enhanced gas sensing properties along with remarkable recovery kinetics. For instance, Cui *et al.* [111] demonstrated MoS₂/SnO₂ hybrid for NO₂ detection at room temperature with complete recovery without any external stimulus. These authors observe that the relatively weaker binding (when compared to pristine MoS₂) between the sensing material (due to presence of SnO₂) and NO₂ gas molecules facilitate complete recovery at room temperature. Therefore, it is very likely that the presence of MoO₃ on the surface of MoS₂ mitigates the problem of incomplete recovery at room temperature. Finally, it is important to point out that, regardless of any performance metrics, we have achieved BEOL-compatible MoS₂ sensing functionality [17, 18], with reduced energy consumption. This meets the objective of creating diverse functionality for More-than-Moore integration.

4. Conclusions

Repeatable and rapid MoS₂ growth (~1–10 nm) on SiO₂, glass, a-Al₂O₃ and c-plane sapphire is achieved by CVD at 350–550 °C in a manufacturing-compatible 300 mm ALD reactor, which is approximately at and below the BEOL thermal budget limit. The formation of polycrystalline MoS₂ is confirmed by various structural and chemical characterisation techniques. Macro-scale Hall/4P measurements on the ~10 nm MoS₂ films, which have rarely been reported in the literature, indicate high 4-point resistivity (~1.4–3.3 kΩ cm), very low Hall carrier concentrations (10¹⁴–10¹⁵ cm⁻³), and a Hall mobility of 0.5–17 cm² V⁻¹ s⁻¹. Independent micro-scale c-TLM resistor and field-effect transistor analysis corroborate the macro-scale 4P resistivity and DC Hall carrier concentration and mobility results. In terms of logic devices, due to the low thermal budget growth, the gating of lateral transport is limited, and further work is required based on MoS₂ doping or functionalisation. However, the MoS₂ films do exhibit memory and sensing functions. For BEOL memory, vertical transport structures (Au/MoS₂/Au) based on ~3 nm thick 550°C-grown (~0.75 hours) MoS₂ films show memristive switching and a stable memory window of 10⁵ between the high and low resistive states, with a retention time of > 10⁴ seconds. The switching set and reset voltages in these memristors demonstrate a significant reduction compared to memristors fabricated from pristine, single-crystalline MoS₂ at higher temperatures, thereby reducing the energy needed for operation. For BEOL sensing, the ~5 nm thick, 550 °C-grown (~1.25 hours), MoS₂ films incorporated into an inter-digitated electrode-based gas sensing platform exhibit a highly selective response along with a sub-ppm level sensitivity to NO₂ gas. The excellent

recovery to the baseline at room temperature without the need for additional energy input improves the financial and energy cost, shelf life and carbon footprint. The demonstration of large-area direct growth of uniform, continuous, and repeatable 2H-phase polycrystalline MoS₂ within a BEOL thermal budget, alongside memristive and gas sensing functionality, advances a key enabling technology objective in emerging materials and devices for 3D heterogeneous integration.

Acknowledgements

The authors acknowledge the financial support of Science Foundation Ireland through the projects *ATOM² (SFI-TP32AMBER-ATOM2)*, *INVEST (SFI-15/IA/3131)*, and the *AMBER Research Centres (12/RC/2278)*. The authors would like to acknowledge the helpful comments and suggestions of Dr. Cormac Ó Coileáin, Trinity College Dublin, Ireland. LAW would like to acknowledge funding from the European Union's *Horizon 2020* research and innovation program under the Marie Skłodowska-Curie Actions grant agreement No. 713567. GSD would like to acknowledge funding from the European Union's *Horizon 2020* research and innovation project *QUEFORMAL* under grant agreement No. 829035. We acknowledge funding support from the Ministry of Human Resource Development (MHRD), India; the Department of Electronics and Information Technology (DeITY), India; the Department of Science and Technology's (DST's) Nanomission through the Nanoelectronics Network for Research and Application (NNetRA). We also acknowledge the technical support provided by staff at the National Nano Fabrication Facility (NNFC), Centre for Nano Science and Engineering (CeNSE), the Indian Institute of Science (IISc), Bangalore, India. NB would also like to thank the Indian National Academy of Engineering (INAE), and the Science and Engineering Research Board (SERB), for the Technology Innovation National Fellowship of Abdul Kalam.

References

- [1] Bae S *et al* 2010 Roll-to-roll production of 30-inch graphene films for transparent electrodes *Nat. Nanotechnol.* **5** 574-578
- [2] Backes C *et al* 2020 Production and processing of graphene and related materials *2D Mater.* **7** 022001
- [3] Li L, Zhu Z, Wang T, Currivan-Incorvia J A, Yoon A and Wong H-S P 2016 BEOL compatible graphene/Cu with improved electromigration lifetime for future interconnects *IEEE International Electron Devices Meeting (IEDM) (San Francisco, CA, USA, December 3-7) 9.5.1-9.5.4*
- [4] Mak K F and Sha J 2016 Photonics and optoelectronics of 2D semiconductor transition metal dichalcogenides *Nat. Photonics* **10** 216-226
- [5] Duan X, Wang C, Pan A, Yu R and Duan X 2015 Two-dimensional transition metal dichalcogenides as atomically thin semiconductors: opportunities and challenges *Chem. Soc. Rev.* **44** 8859-8876

- [6] Ansari L *et al* 2019 Quantum confinement-induced semimetal-to-semiconductor evolution in large-area ultra-thin PtSe₂ films grown at 400 °C *npj 2D Mater. Appl.* **3** 33
- [7] Desai S B *et al* 2016 MoS₂ transistors with 1-nanometer gate lengths *Science* **354** 99-102
- [8] Di Bartolomeo A, Genovese L, Foller T, Giubileo F, Luongo G, Croin L, Liang S J, Ang L K and Schleberger M 2017 Electrical transport and persistent photoconductivity in monolayer MoS₂ phototransistors *Nanotechnology* **28** 214002
- [9] He X P and Tian H 2016 Photoluminescence architectures for disease diagnosis: from graphene to thin-layer transition metal dichalcogenides and oxides *Small* **12** 144-160
- [10] Chhowalla M, Shin H S, Eda G, Li L-J, Loh K P and Zhang H 2013 The chemistry of two-dimensional layered transition metal dichalcogenide nanosheets *Nature Chem.* **5** 263-275
- [11] Zeng M, Xiao Y, Liu J, Yang K and Fu L 2018 Exploring two-dimensional materials toward the next-generation circuits: from monomer design to assembly control *Chem. Rev.* **118** 6236-6296
- [12] Lee K, Gatensby R, McEvoy N, Hallam T and Duesberg G S 2013 High performance sensors based on molybdenum disulfide thin films *Adv. Mater.* **25** 6699-6702
- [13] Briggs N *et al* 2019 A roadmap for electronic grade 2D materials *2D Mater.* **6** 022001
- [14] Kozhakhmetov A, Nasr J R, Zhang F, Xu K, Briggs N C, Addou R, Wallace R, Fullerton-Shirey S K, Terrones M, Das S and Robinson J A 2020 Scalable BEOL compatible 2D tungsten diselenide *2D Mater.* **7** 015029
- [15] Fenouillet-Beranger C *et al* 2014 New insights on bottom layer thermal stability and laser annealing promises for high performance 3D VLSI *IEEE International Electron Devices Meeting (IEDM) (San Francisco, CA, USA, December 15-17)* 27.5.1-27.5.4
- [16] Yim C *et al* 2016 High-performance hybrid electronic devices from layered PtSe₂ films grown at low temperature *ACS Nano* **10** 9550-9558
- [17] IEEE International Roadmap for Devices and Systems (IEEE IRDS, <https://irds.ieee.org>), 2018 Edition, Executive Summary: "...goal is to pursue long-term alternative solutions to technologies addressed in More-than-Moore (MtM)..."; and in the Beyond CMOS report: "...beyond-CMOS devices include those related to memory technologies, ...logic devices, and heterogeneous integration of More-than-Moore (MtM) or Functional Diversification"; incl. Table BC 1.1: "...heterogeneously integrable with CMOS...incorporating functionalities that do not necessarily scale according to Moore's Law".
- [18] IEEE Heterogeneous Integration Roadmap (IEEE HIR, see <http://eps.ieee.org/hir>) on materials and devices, 2019 Edition, HIR Overview and Executive Summary
- [19] Sankar I V, Jeon J, Jang S K, Cho J H, Hwang E and Lee S 2019 Heterogeneous integration of 2D materials: recent advances in fabrication and functional device applications *Nano* **14** 1930009
- [20] McClellan C, Bailey C, Datye I, Gabourie A, Grady R, Schauble K, Vaziri S and Pop E 2019 3D heterogeneous integration with 2D materials *Silicon Nanoelectronics Workshop (SNW) (Kyoto, Japan, June 9-10)* 1-2
- [21] Ayari A, Cobas E, Ogundadegbe O and Fuhrer M S 2007 Realization and electrical characterization of ultrathin crystals of layered transition-metal dichalcogenides *J. Appl. Phys.* **101** 014507
- [22] Radisavljevic B, Radenovic A, Brivio J, Giacometti V and Kis A 2011 Single-layer MoS₂ transistors *Nat. Nanotechnol.* **6** 147-150
- [23] Liu H, Neal A T and Ye P D 2012 Channel length scaling of MoS₂ MOSFETs *ACS Nano* **6** 8563-8569
- [24] Kim S *et al* 2012 High-mobility and low-power thin-film transistors based on multilayer MoS₂ crystals *Nat. Commun.* **3**:1011
- [25] Huyghebaert C *et al* 2018 2D materials: roadmap to CMOS integration *IEEE International Electron Devices Meeting (IEDM) (San Francisco, CA, USA, December 1-5)* 22.1.1-22.1.4
- [26] Kim T, Mun J, Park H, Joung D, Diware M, Won C, Park J, Jeong S-H and Kang S-W 2017 Wafer-scale production of highly uniform two-dimensional MoS₂ by metal-organic chemical vapor deposition *Nanotechnology* **28** 18LT01
- [27] Gong Y *et al* 2015 Tellurium-assisted low-temperature synthesis of MoS₂ and WS₂ monolayers *ACS nano* **9** 11658-11666
- [28] Kang K, Xie S, Huang L, Han Y, Huang P Y, Mak K F, Kim C J, Muller D and Park J 2015 High-mobility three-atom-thick semiconducting films with wafer-scale homogeneity *Nature* **520** 656-660
- [29] Lee Y H *et al* 2012 Synthesis of large-area MoS₂ atomic layers with chemical vapor deposition *Adv. Mater.* **24** 2320-2325
- [30] Chen C, Qiao H, Xue Y, Yu W, Song J, Lu Y, Li S and Bao Q 2015 Growth of large-area atomically thin MoS₂ film via ambient pressure chemical vapor deposition *Photonics Res.* **3** 110-114
- [31] Zheng W, Qiu Y, Feng W, Chen J, Yang H, Wu S, Jia D, Zhou Y and Hu P 2017 Controlled growth of six-point stars MoS₂ by chemical vapor deposition and its shape evolution mechanism *Nanotechnology* **28** 395601
- [32] Mun J, Kim Y, Kang I S, Lim S K, Lee S J, Kim J W, Park H M, Kim T and Kang S W 2016 Low-temperature growth of layered molybdenum disulphide with controlled clusters. *Sci. Rep.* **6** 21854
- [33] O'Brien M, McEvoy N, Hallam T, Kim H Y, Berner N C, Hanlon D, Lee K, Coleman J N and Duesberg G S 2014 Transition metal dichalcogenide growth via close proximity precursor supply *Sci. Rep.* **4** 7374
- [34] Bergeron H, Sangwan V K, McMorro J J, Campbell G P, Balla I, Liu X, Bedzyk M J, Marks T J and Hersam M C 2017 Chemical vapor deposition of monolayer MoS₂ directly on ultrathin Al₂O₃ for low-power electronics *Appl. Phys. Lett.* **110** 053101
- [35] Kumar V K, Dhar S, Choudhury T H, Shivashankar S A and Raghavan S 2015 A Predictive approach to CVD of crystalline layers of TMDs: the case of MoS₂ *Nanoscale* **7** 7802-7810
- [36] Liu X, Chai Y and Liu Z 2017 Investigation of chemical vapour deposition MoS₂ field effect transistors on SiO₂ and ZrO₂ substrates *Nanotechnology* **28** 164004
- [37] Yu Y, Li C, Liu Y, Su L, Zhang Y and Cao L 2013 Controlled scalable synthesis of uniform, high-quality monolayer and few-layer MoS₂ films *Sci. Rep.* **3** 1866

- [38] Najmaei S, Liu Z, Zhou W, Zou X, Shi G, Lei S, Yakobson B I, Idrobo J C, Ajayan P M and Lou J 2013 Vapour phase growth and grain boundary structure of molybdenum disulphide atomic layers *Nat. Mater.* **12** 754-759
- [39] Dumcenco D *et al* 2015 Large-area epitaxial monolayer MoS₂ *ACS Nano* **9** 4611-4620
- [40] Chiappe D *et al* 2018 Layer-controlled epitaxy of 2D semiconductors: bridging nanoscale phenomena to wafer-scale uniformity *Nanotechnology* **29** 425602
- [41] Cun H, Macha M, Kim H, Liu K, Zhao Y, LaGrange T, Kis A and Radenovic A 2019 Wafer-scale MOCVD growth of monolayer MoS₂ on sapphire and SiO₂ *Nano Res.* **12** 2646-2652
- [42] Islam Z, Zhang K, Robinson J and Haque A 2019 Quality enhancement of low temperature metal organic chemical vapor deposited MoS₂: an experimental and computational investigation *Nanotechnology* **30** 395402
- [43] Jang Y, Yeo S, Lee H-B-R, Kim H and Kim S-H 2016 Wafer-scale, conformal and direct growth of MoS₂ thin films by atomic layer deposition *Appl. Surf. Sci.* **365** 160-165
- [44] Mattinen M, Hatanpää T, Sarnet T, Mizohata K, Meinander K, King P J, Khriachtchev L, Räisänen J, Ritala M and Leskelä M 2017 Atomic layer deposition of crystalline MoS₂ thin films: new molybdenum precursor for low-temperature film growth *Adv. Mater. Interfaces* **4** 1700123
- [45] Browning R, Padigi P, Solanki R, Tweet D J, Schuele P and Evans D 2015 Atomic layer deposition of MoS₂ thin films *Mater. Res. Express* **2** 035006
- [46] Liu L, Huang Y, Sha J and Chen Y 2017 Layer-controlled precise fabrication of ultrathin MoS₂ films by atomic layer deposition *Nanotechnology* **28** 195605
- [47] Pyeon J J, Kim S H, Jeong D S, Baek S-H, Kang C-Y, Kim J-S and Kim S K 2016 Wafer-scale growth of MoS₂ thin films by atomic layer deposition *Nanoscale* **8** 10792
- [48] Jin Z, Shin S, Kwon D H, Han S-J and Min Y-S 2014 Novel chemical route for atomic layer deposition of MoS₂ thin film on SiO₂/Si substrate *Nanoscale* **6** 14453
- [49] Tan L K, Liu B, Teng J H, Guo S, Low H Y and Loh K P 2014 Atomic layer deposition of a MoS₂ film *Nanoscale* **6** 10584-10588
- [50] Valdivia A, Tweet D J and Conley Jr J F 2016 Atomic layer deposition of two dimensional MoS₂ on 150 mm substrates *J. Vac. Sci. Technol. A* **34** 021515
- [51] Jurca T, Moody M J, Henning A, Emery J-D, Wang B, Tan J M, Lohr T L, Lauhon L J and Marks T J 2017 Low-temperature atomic layer deposition of MoS₂ films *Angew. Chem. Int. Ed.* **56** 4991-4995
- [52] Subramanian S, Briggs N, Shallenberger J, Wetherington M T and Robinson J A 2020 Caveats in obtaining high-quality 2D materials and property characterization *Journal of Materials Research* **35** 855-863
- [53] Sangwan V K, Lee H S, Bergeron H, Balla I, Beck M E, Chen K S and Hersam M C 2018 Multi-terminal memtransistors from polycrystalline monolayer molybdenum disulfide *Nature* **554** 500-504
- [54] Li D, Wu B, Zhu X, Wang J, Ryu B, Lu W D, Lu W and Liang X 2018 MoS₂ memristors exhibiting variable switching characteristics toward biorealistic synaptic emulation *ACS Nano* **12** 9240-9252
- [55] Ge R, Wu X, Kim M, Shi J, Sonde S, Tao L, Zhang Y, Lee J C, Akinwande D 2018 Atomistor: nonvolatile resistance switching in atomic sheets of transition metal dichalcogenides *Nano Lett.* **18** 434-441
- [56] Xu R, Jang H, Lee M H, Amanov D, Cho Y, Kim H, Park S, Shin H J and Ham D 2019 Vertical MoS₂ double-layer memristor with electrochemical metallization as an atomic-scale synapse with switching thresholds approaching 100 mV *Nano Lett.* **19** 2411-2417
- [57] Zhao H *et al* 2017 Atomically Thin Femtojoule Memristive Device *Adv. Mater.* **29** 1703232
- [58] Wu X, Ge R, Chen P-A, Chou H, Zhang Z, Zhang Y, Banerjee S, Chiang M-H, Lee J C and Akinwande D 2019 Thinnest nonvolatile memory based on monolayer h-BN *Adv. Mater.* **31** 1806790
- [59] Bhattacharjee S *et al* 2020 Insights into multilevel resistive switching in monolayer MoS₂ *ACS Appl. Mater. Interfaces* **12** 6022-6029
- [60] Cho B *et al* 2015 Charge-transfer-based gas sensing using atomic-layer MoS₂ *Sci. Rep.* **5** 8052
- [61] Kang M A, Han J K, Cho S Y, Bu S D, Park C Y, Myung S, Song W, Lee S S, Lim J and An K S 2017 Strain-gradient effect in gas sensors based on three-dimensional hollow molybdenum disulfide nanoflakes *ACS Appl. Mater. & interfaces* **9** 43799-806
- [62] Cho B *et al* 2015 Bifunctional sensing characteristics of chemical vapor deposition synthesized atomic-layered MoS₂ *ACS applied materials & interfaces* **7** 2952-2959
- [63] Kumar R, Kulriya P K, Mishra M, Singh F, Gupta G and Kumar M 2018 Highly selective and reversible NO₂ gas sensor using vertically aligned MoS₂ flake networks *Nanotechnology* **29** 464001
- [64] Zhao Y *et al* 2018 Low-temperature synthesis of 2D MoS₂ on a plastic substrate for a flexible gas sensor *Nanoscale* **10** 9338-45
- [65] Goel N, Kumar R and Kumar M 2018 Enhanced sensing response with complete recovery of MoS₂ sensor under photoexcitation *AIP Conference Proceedings* **1942** 050060
- [66] Agrawal A V, Kumar R, Venkatesan S, Zakhidov A, Yang G, Bao J, Kumar M and Kumar M 2018 Photoactivated mixed in-plane and edge-enriched p-type MoS₂ flake-based NO₂ sensor working at room temperature *ACS Sens.* **3** 998-1004
- [67] Kumar R, Goel N and Kumar M 2017 UV-activated MoS₂ based fast and reversible NO₂ sensor at room temperature *ACS Sens.* **2** 1744-1752
- [68] Xu T, Pei Y, Liu Y, Wu D, Shi Z, Xu J, Tian Y and Li X 2017 High-response NO₂ resistive gas sensor based on bilayer MoS₂ grown by a new two-step chemical vapor deposition method. *J. Alloys Compd.* **725** 253-259
- [69] Pham T, Li G, Bekyarova E, Itkis M E and Mulchandani A 2019 MoS₂-based optoelectronic gas sensor with sub-parts-per-billion limit of NO₂ gas detection *ACS Nano* **13** 3196-3205
- [70] Cho S Y, Kim S J, Lee Y, Kim J S, Jung W B, Yoo H W, Kim J and Jung H T 2015 Highly enhanced gas adsorption properties in vertically aligned MoS₂ layers *ACS Nano* **9** 9314-21
- [71] Kang Y, Pyo S, Jo E and Kim J 2019 Light-assisted recovery of reacted MoS₂ for reversible NO₂ sensing at room temperature *Nanotechnology* **30** 355504

- [72] Guo J, Wen R, Zhai J and Wang Z L 2019 Enhanced NO₂ gas sensing of a single-layer MoS₂ by photogating and piezo-phototronic effects *Science Bulletin* **64** 128-135
- [73] Perkins F K, Friedman A L, Cobas E, Campbell P M, Jernigan G G and Jonker B T 2013 Chemical vapor sensing with monolayer MoS₂ *Nano Lett.* **13** 668-673
- [74] Cho B *et al* 2015 Chemical sensing of 2D graphene/MoS₂ heterostructure device *ACS Appl. Mater. Interfaces* **7** 16775-16780
- [75] Liu B, Chen L, Liu G, Abbas AN, Fathi M and Zhou C 2014 High-performance chemical sensing using Schottky-contacted chemical vapor deposition grown monolayer MoS₂ transistors *ACS Nano* **8** 5304-14
- [76] Long H, Harley-Trochimczyk A, Pham T, Tang Z, Shi T, Zettl A, Carraro C, Worsley M A and Maboudian R 2016 High surface area MoS₂/graphene hybrid aerogel for ultrasensitive NO₂ detection *Adv. Funct. Mater.* **26** 5158-5165
- [77] Long H, Chan L, Harley-Trochimczyk A, Luna L E, Tang Z, Shi T, Zettl A, Carraro C, Worsley M A and Maboudian R 2017 3D MoS₂ aerogel for Ultrasensitive NO₂ detection and its tunable sensing behavior *Adv. Mater. Interfaces* **4** 1700217
- [78] Lin J *et al* 2018 Large area growth of non-intentionally doped MoS₂ in a 300 mm atomic layer deposition reactor *Joint International EUROSIOI Workshop and International Conference on Ultimate Integration on Silicon (EUROSIOI-ULIS) (Granada, Spain, March 19-21) session 4*
- [79] Shulaker M M, Hills G, Park R S, Howe R T, Saraswat K, Wong H S P and Mitra S 2017 Three-dimensional integration of nanotechnologies for computing and data storage on a single chip *Nature* **547** 74-78
- [80] Sakhuja N, Jha R K, Chaurasiya R, Dixit A and Bhat N 2010 1T-Phase Titanium Disulfide Nanosheets for Sensing H₂S and O₂ *ACS Appl. Nano Mater.* **3** 3382-3394
- [81] Vilá R A, Momeni K, Wang Q, Bersch B M, Lu N, Kim M J, Chen L Q and Robinson J A 2016 Bottom-up synthesis of vertically oriented two-dimensional materials *2D Mater.* **3** 041003
- [82] Neal A T, Pachter R and Mou S 2017 P-type conduction in two-dimensional MoS₂ via oxygen incorporation *Appl. Phys. Lett.* **110** 193103
- [83] Mignuzzi S, Pollard A J, Bonini N, Brennan B, Gilmore I S, Pimenta M A, Richards D and Roy D 2015 Effect of disorder on Raman scattering of single-layer MoS₂ *Phys. Rev. B* **91** 195411
- [84] Lee C, Yan H, Brus L E, Heinz T F, Hone J and Ryu S 2010 Anomalous lattice vibrations of single- and few-layer MoS₂ *ACS Nano* **4** 2695-2700
- [85] Attanayake N H *et al* 2017 Effect of intercalated metals on the electrocatalytic activity of 1T-MoS₂ for the hydrogen evolution reaction *ACS Energy Lett.* **3** 7-13
- [86] Knirsch K C *et al* 2015 Basal-Plane Functionalization of Chemically Exfoliated Molybdenum Disulfide by Diazonium Salts *ACS Nano* **9** 6018-6030
- [87] Wang Y, He R, Su M and Xie W 2017 Synthesis of the few layered two-dimensional molybdenum oxide atomic crystal *IOP Conf. Ser.: Mater. Sci. Eng.* **167** 012020
- [88] Vangelista S, Cinquanta E, Martella C, Alia M, Longo M, Lamperti A, Mantovan R, Basset F B, Pezzoli F and Molle A 2016 Towards a uniform and large-scale deposition of MoS₂ nanosheets via sulfurization of ultra-thin Mo-based solid films *Nanotechnology* **27** 175703
- [89] Schroder D K 2006 *Semiconductor Material and Device Characterization* 3rd Ed. (John Wiley & Sons Inc., Hoboken, New Jersey, USA)
- [90] Lu C-P, Li G, Mao J, Wang L-M and Andrei E Y 2014 Bandgap, mid-gap states, and gating effects in MoS₂ *Nano Lett.* **14** 4628-4633
- [91] Zou X, Liu Y and Yakobson B I 2013 Predicting dislocations and grain boundaries in two-dimensional metal-disulfides from the first principles *Nano Lett.* **13** 253-258
- [92] Seto J Y W 1975 The electrical properties of polycrystalline silicon films *J. Appl. Phys.* **46** 5247-5254
- [93] O'Mara W C, Herring R B, Hunt L P 1990 *Handbook of Semiconductor Silicon Technology* (Noyes Publications: Park Ridge, New Jersey, USA) p 684-711
- [94] Gao J, Li B, Tan J, Chow P, Lu T M and Koratkar N 2016 Aging of transition metal dichalcogenide monolayers *ACS Nano* **10** 2628-2635
- [95] Zhao R, Lo C-L, Zhang F, Ghosh R K, Knobloch T, Terrones M, Chen Z and Robinson J 2019 Incorporating niobium in MoS₂ at BEOL-compatible temperatures and its impact on copper diffusion barrier performance *Adv. Mater. Interfaces* **6** 1901055
- [96] Presolski S and Pumera M 2016 Covalent functionalization of MoS₂ *Mater. Today* **19** 140-145
- [97] Hallam T, Monaghan S, Gity F, Ansari L, Schmidt M, Downing C, Cullen C P, Nicolosi V, Hurley P K and Duesberg G S 2017 Rhenium-doped MoS₂ films *Appl. Phys. Lett.* **111** 203101
- [98] Kim H, Kim W, O'Brien M, McEvoy N, Yim C, Marcia M, Hauke F, Hirsch A, Kim G T and Duesberg G S 2018 Optimized single-layer MoS₂ field-effect transistors by non-covalent functionalisation *Nanoscale* **10** 17557-17566
- [99] Zhang T and Fu L 2018 Controllable chemical vapor deposition growth of two-dimensional heterostructures *Chem* **4** 671-689
- [100] Wang M *et al* 2018 Robust memristors based on layered two-dimensional materials *Nat. Electron.* **1** 130-136
- [101] Kim M, Ge R, Wu X, Lan X, Tice J, Lee J C and Akinwande D 2018 Zero-static power radio-frequency switches based on MoS₂ atomristors *Nat. Commun.* **9** 2524
- [102] Waser R and Aono M 2007 Nanoionics-based resistive switching memories *Nat. Mater.* **6** 833-840.
- [103] Suñé J, Raghavan N and Pey K L 2016 *Dielectric Breakdown Processes*, Chapter 8 of "Resistive switching: from fundamentals of nanoionic redox processes to memristive device applications" (Eds: Ielmini D and Waser R) (Wiley-VCH, Weinheim, Germany) p 232-233
- [104] Donarelli M, Bisti F, Perrozzi F and Ottaviano L 2013 Tunable sulfur desorption in exfoliated MoS₂ by means of thermal annealing in ultra-high vacuum *Chem. Phys. Lett.* **588** 198-202
- [105] Yue Q, Chang S, Qin S and Li J 2013 Functionalization of monolayer MoS₂ by substitutional doping: a first-principles study *Phys. Lett. A* **377** 1362-1367
- [106] Dolui K, Rungger I, Das Pemmaraju C and Sanvito S 2013 Possible doping strategies for MoS₂ monolayers: an ab initio study *Phys. Rev. B* **88** 075420

- [107] Ramanathan A A 2018 Defect functionalization of MoS₂ nanostructures as toxic gas sensors: A review *IOP Conference Series: Materials Science and Engineering* **305** 012001
- [108] Zhao S, Xue J and Kang W 2014 Gas adsorption on MoS₂ monolayer from first-principles calculations *Chem. Phys. Lett.* **595** 35-42
- [109] Qin Z, Xu K, Yue H, Wang H, Zhang J, Ouyang C, Xie C and Zeng D 2018 Enhanced room-temperature NH₃ gas sensing by 2D SnS₂ with sulfur vacancies synthesized by chemical exfoliation *Sensors and Actuators B: Chemical* **262** 771-779
- [110] Kumar R, Goel N, Mishra M, Gupta G, Fanetti M, Valant M and Kumar M 2018 Growth of MoS₂-MoO₃ hybrid microflowers via controlled vapor transport process for efficient gas sensing at room temperature. *Advanced Materials Interfaces* **5**, no. 10: 1800071
- [111] Cui S, Wen Z, Huang X, Chang J and Chen J 2015 Stabilizing MoS₂ nanosheets through SnO₂ nanocrystal decoration for high-performance gas sensing in air." *Small* **11**, no. 19: 2305-2313